Reversible adsorption and confinement of nitrogen dioxide within a Robust Porous Metal-Organic Framework

Xue Han,[1] Harry G.W. Godfrey,[1] Lydia Briggs,[1] Andrew J. Davies,[2] Yongqiang Cheng,[3] Luke L. Daemen,[3] Alena M. Sheveleva,[1,4] Floriana Tuna,[1] Eric J.L. McInnes,[1] Junliang Sun,[5] Christina Drathen,[6] Michael W. George,[2,7] Anibal J. Ramirez-Cuesta,[3] K. Mark Thomas[8] Martin Schröder[1]* and Sihai Yang,[1]*

[1] School of Chemistry, University of Manchester, Manchester, M13 9PL (UK)

[2] School of Chemistry, University of Nottingham, University Park, Nottingham, NG7 2RD (UK)

[3] The Chemical and Engineering Materials Division (CEMD), Neutron Sciences Directorate, Oak Ridge National Laboratory, Oak Ridge, TN 37831 (USA)

[4] International Tomography Center SB RAS and Novosibirsk State University, Novosibirsk, 630090 (Russia)

[5] College of Chemistry and Molecular Engineering, Peking University, Beijing, 100871 (China)

[6] European Synchrotron Radiation Facility, Grenoble, 38043 (France)

[7] Department of Chemical and Environmental Engineering, University of Nottingham Ningbo China, Ningbo, 315100 (China)

[8] Northern Carbon Research Laboratories, School of Chemical Engineering and Advanced Materials, University of Newcastle upon Tyne, Newcastle upon Tyne, NE1 7RU (UK)

Nitrogen dioxide (NO$_2$) is a major air pollutant causing significant environmental problems[1,2] and premature death[3,4]. We report the first example of reversible adsorption of NO$_2$ in a robust metal-organic framework. At ambient conditions, MFM-300(Al) exhibits a reversible NO$_2$ isotherm uptake of 14.1 mmol/g, and, more importantly, an exceptional performance of selective removal of low concentration NO$_2$ (5000 to <1 ppm) from gas mixtures. Complementary experiments reveal five types of supramolecular interactions cooperatively binding both NO$_2$ and N$_2$O$_4$ molecules within MFM-300(Al). We find that the *in situ* equilibrium 2NO$_2$↔N$_2$O$_4$ within the pores is pressure-independent, whereas *ex situ* in unrestricted space this equilibrium is an exemplar first-order process dependent upon pressure. The unusual co-existence of helical monomer-dimer chains of NO$_2$ in MFM-300(Al) offers a new fundamental understanding of the chemical properties of guest within porous hosts, and successful breakthrough experiments pave the way for the development of future capture and conversion technologies.

NO$_2$ is the most prevalent form of NO$_x$ that is generated by anthropogenic activities and is an important feedstock for chemical industry. Mitigation of NO$_x$ pollution is a complex issue, not least because of its highly reactive, oxidizing and corrosive nature[5]. Physisorption of gases by porous materials using supramolecular host-guest interactions is a promising approach that can give high reversibility and low energy penalty for system regeneration, and zeolites[6], metal oxides[7], mesoporous silica[8] and activated carbons[9,10] have been investigated for NO$_2$ adsorption. However, these materials suffer from low adsorption capacities and the high reactivity of NO$_2$ often affords irreversible uptake within these porous solids, leading to disproportionation to NO$^+$ and NO$_3^-$ coupled with oxidation and degradation of the interior of the host material[6-10].

Porous metal-organic frameworks (MOFs) are emerging solid adsorbents[11], but isothermal adsorption of NO$_2$ in MOFs has not been reported. Additionally, experimental insights into the nature of NO$_2$···host interactions at surface sites and NO$_2$···NO$_2$ interactions within confined nano-pores are rarely explored and poorly understood. Herein, we describe an ultra-robust material, MFM-300(Al), showing unprecedented reversible and selective adsorption of NO$_2$. MFM-300(Al) can be fully regenerated post adsorption without loss of crystallinity or porosity. We also report the application of high resolution synchrotron X-ray powder diffraction (PXRD), Fourier transform infrared (FTIR), electron paramagnetic resonance (EPR) and inelastic neutron spectroscopy (INS) coupled with density functional theory (DFT) and molecular dynamic (MD) calculations to directly visualise the binding domains, dynamics of host-guest interactions, reactivity and chemical behaviour of adsorbed NO$_2$ within MFM-300(Al). These complementary experiments using dynamic, kinetic and static approaches reveal five different types of soft supramolecular interactions cooperatively binding both NO$_2$ and N$_2$O$_4$ molecules within the functionalized cavities of MFM-300(Al). The cooperativity of these soft interactions directly explains the optimal uptake and selectivity for NO$_2$ in MFM-300(Al).

MFM-300(Al) was selected for the study of NO_2 adsorption because of its exceptional stability[12]. At 298 K, the maximum NO_2 isotherm uptake in MFM-300(Al) was measured as 14.1 mmol g^{-1} (64.9 wt% or 316 cm^3 g^{-1}/STP) at 1.0 bar (Fig. 1a). This uptake is much higher than values reported for modified Y zeolites[6], mixed oxides $Ce_{1-x}Zr_xO_2$[7], amine-functionalized SBA-15[8], urea-modified mesoporous carbons[9], and activated carbons[10]. Although the NO_2 capacities of a number of MOFs[13-16], metal-doped MOFs[17] and MOF/graphite oxide composites[18,19] have been estimated from (micro)breakthough experiments using mixtures of gases containing 1000-2000 ppm of NO_2 (Table S4), these cannot be compared with the direct uptakes obtained here *via* isotherm experiments with pure NO_2 (see SI). Significantly, the NO_2 uptake in MFM-300(Al) is fully reversible, and the host material can be regenerated with full retention of structure and porosity for at least 5 cycles (Fig. S2). The isosteric heats of adsorption (Q_{st}) of NO_2 in MFM-300(Al) is *ca.* 50 kJ mol^{-1} at a surface coverage of 2-8 mmol g^{-1}. The absence of notable variation of Q_{st} as a function of surface coverage indicates the presence of uniform host-guest and guest-guest interactions. The binding energy of NO_2 in MFM-300(Al) has also been obtained by DFT calculations at a loading of 14.5 mmol g^{-1} (equivalent to $3NO_2$/Al), to be 44 kJ mol^{-1}.

We were interested to analyse the IAST selectivity of NO_2 with respect to other components of exhaust gases SO_2, CO_2 and N_2 (Figs. 1c, S29). At 298 K and 1 bar, MFM-300(Al) shows a selectivity of 18.1, 248 and >10,000 for NO_2/SO_2, NO_2/CO_2 and NO_2/N_2 mixtures, respectively. The adsorptive removal of low concentrations of NO_2 by MFM-300(Al) has been confirmed in breakthrough experiments in which a stream of NO_2 (5000 ppm diluted in He/N_2) was flowed over a packed bed of MFM-300(Al) under ambient conditions (Fig. 1d). As expected, He and N_2 were the first to elute through the bed (dimensionless time = 180), whereas NO_2 was selectively retained. Upon saturation (dimensionless time >5000), NO_2 breaks through from the bed and reaches saturation rapidly. As measured from this breakthrough experiment, for an entering feed of 5000 ppm NO_2, the NO_2 composition can be purified to below 1 ppm (below the detection limit of the mass spectrometry) until the breakthrough. The capability of MFM-300(Al) to capture NO_2 in presence of moisture has been demonstrated by breakthrough experiments using wet NO_2 gas stream (Fig. 1d). In presence of water vapour, the breakthrough of NO_2 from MFM-300(Al) slightly reduced to 4600 (dimensionless time) as a result of competitive adsorption of water. The selective retention of NO_2 by MFM-300(Al) has also been confirmed in competitive breakthrough experiments using gas mixtures containing CO_2 or SO_2 (Figs. 1e-f). In both cases, CO_2 and SO_2 were the first to elute through the bed and NO_2 was selectively retained in the bed until breakthrough, consistent with the estimation of adsorption selectivity data. Thus these results from static and dynamic adsorption experiments both indicate the potential of utilizing MFM-300(Al) for NO_2 capture.

The density of adsorbed NO_2 molecules in MFM-300(Al) is estimated to be 1.73 g cm^{-3} at 298 K and 1.0 bar. Interestingly, this is higher than that of liquid NO_2 and N_2O_4 (1.45 g cm^{-3} and 1.44 g cm^{-3}, respectively, at 294 K), but lower than that of solid N_2O_4 (1.94 g cm^{-3} at 140 K)[20] suggesting highly efficient packing of NO_2 molecules in the

pore. Synchrotron powder X-ray diffraction (PXRD) data collected upon NO_2 adsorption at 298 K revealed two independent binding sites (I and II, assigned as NO_2 and N_2O_4 molecules, respectively) within the pore of MFM-300(Al). The final structural model for MFM-300(Al)·$(NO_2)_2$·$(N_2O_4)_2$ has been validated by Rietveld refinement and DFT calculations (Figs. 2). The total crystallographic occupancy of NO_2 molecules (2.82 NO_2/Al) is in excellent agreement with that obtained from the isotherm experiment (2.92 NO_2/Al) at the same temperature and pressure. The NO_2 molecules at site I (occupancy = 1.00) exhibit an end-on interaction to the HO-Al group *via* formation of moderate-to-weak hydrogen bonds ($O^{NO2}\cdots HO$ = 2.00 Å) that are supplemented by additional four-fold supramolecular contacts of the O(δ-) centre of NO_2 to the aromatic hydrogen atoms (δ+) (O$\cdots$HC = 2.62, 2.66, 3.35, 3.40 Å) and a strong dipole interaction between the N(δ-) centre of NO_2 molecule and the C(δ+) centre of the carboxylate group (N$\cdots$C = 3.11 Å). N_2O_4 molecules (occupancy = 0.91) at site II are located in the middle of the pore and interact primarily with the NO_2 molecules at site I *via* a three-fold intermolecular dipole interactions ($N^d\cdots O^m$ = 3.80-3.91 Å). In addition, N_2O_4 molecules at site II form intermolecular dipole interactions with adjacent N_2O_4 molecules ($N^d\cdots O^d$ = 2.95, 3.08 Å); these are comparable to those observed in solid N_2O_4 ($N^I\cdots O^{II}$ = 3.13 Å) studied by neutron diffraction at 20 K[20], confirming that the adsorbed N_2O_4 in MFM-300(Al) has a restricted solid-state type arrangement. Thus, in total, five types of weak interactions interact cooperatively to bind NO_2 molecules (up to nine individual contacts; Fig. 2b) within the functionalized cavity.

The alternate presence of NO_2 and N_2O_4 molecules at sites I and II affords a distinct 1D helical $(NO_2\cdot N_2O_4)_\infty$ chain running along the channel of MFM-300(Al) (Fig. 2c). These 1D chains are stabilized by multiple weak intermolecular dipole interactions originated by monomer$\cdots$dimer and dimer$\cdots$dimer. Importantly, the unusual stability of the $(NO_2\cdot N_2O_4)_\infty$ chain within MFM-300(Al) has also been confirmed by molecular dynamics modelling, which suggests that between room temperature and 600 K, the chain in the MOF remains stable within the simulation timescale (10ps), whereas the chain outside the MOF matrix will collapse entirely. Interestingly, locations of adsorbed NO_2 molecules have been determined in a 1D compound [$Rh_2(bza)_4(pyz)$] (bza$^-$ = benzoate; pyz = pyrazine), where all adsorbed NO_2 molecules are found in the dimeric form and no notable guest-guest interaction was observed[21]. Recently, locations of adsorbed NO_2 molecules have also been studied in a zeolite, Ba-Y-FAU, in which three different ionic NO_x species (NO^+, NO^+-NO_2, and NO_3^-) are observed in the pore[22]. In contrast, to our knowledge, the alternating (monomer$\cdots$dimer)$_\infty$ chain described herein represents the first example of co-existence of NO_2 and N_2O_4 molecules within a crystalline matrix.

Inelastic neutron scattering (INS) enabled the direct visualization of the binding dynamics for MFM-300(Al)·$(NO_2)_2$·$(N_2O_4)_2$ with particular focus on the motion of hydrogen atoms involved in the supramolecular contacts. Comparison of INS spectra reveals six major changes in peak intensity on going from bare MFM-300(Al) to MFM-300(Al)·$(NO_2)_2$·$(N_2O_4)_2$ (Figs. 3h-j). Peaks I and II occur at low energy transfer (5-30, 30-60 meV,

respectively) and Peaks III, IV, V and VI at high energy transfer (85, 114, 119-132 and 135-161 meV, respectively).

To understand the changes, simulated INS spectra were obtained *via* DFT calculations based upon the structure model of MFM-300(Al)·$(NO_2)_2$·$(N_2O_4)_2$ and show excellent agreement with experimental spectra (Figs. 2h-j). Peak I corresponds to a series of lattice modes of MFM-300(Al), the decrease in peak intensity being consistent with the NO_2 inclusion. Peaks II and III can be assigned to the deformational modes (*i.e.*, bending and wagging) of –OH groups perpendicular to the Al-O-Al plane and of –CH groups on two benzene rings adjacent to each NO_2 molecule, respectively. Peaks IV and VI can be assigned to out-of-plane and in-plane –CH bending modes, respectively. Finally, peak V corresponds to the in-plane bending modes of the –OH groups. The notable changes observed for Peaks II-VI suggest that adsorbed NO_2 molecules have direct interaction with the -OH and -CH groups, thereby affecting their molecular motions and inducing the changes observed in INS spectra.

In order to probe the phase equilibrium of adsorbed NO_2 and N_2O_4 molecules within MFM-300(Al), the effect of exposing discs of MFM-300(Al) in KBr to varying pressures of NO_2 (0-1 bar) at 298 K was monitored in the region $2760 - 3200$ cm^{-1} by FTIR spectroscopy. Three bands were observed (Fig. 3a), which have previously been assigned[23] to a combination band of NO_2 at 2903 cm^{-1} and combination bands for the dimer, N_2O_4, at 2962 and 3120 cm^{-1}. Fig. 3b shows the IR spectra recorded of MFM-300(Al) exposed to various pressures of NO_2. Several IR peaks due to MFM-300(Al) were also observed in this region, and, therefore, a spectrum recorded under vacuum was used as the background (Fig. 3c). New bands were observed at 2829, 2946 and 3083 cm^{-1} (Fig. 3d), and these increased in intensity with increasing NO_2 pressure. By comparison to the free gas, these new bands were assigned to the formation of adsorbed monomer (NO_2 at 2829 cm^{-1}) and dimer (N_2O_4 at 2946 and 3083 cm^{-1}) within MFM-300(Al). These bands are red-shifted relative to the free gas, and interestingly, the redshift of the monomer band ($\Delta = 74$ cm^{-1}) is significantly larger than those of the dimer ($\Delta = 16, 37$ cm^{-1}), indicating that a stronger host-guest interaction occurs at the monomer site, consistent with the structural model of MFM-300(Al)·$(NO_2)_2$·$(N_2O_4)_2$. The increase in band areas is consistent with the gas adsorption isotherm (Fig. 3f), with bands due to monomer and dimer observed to grow with pressure at approximately the same rate. Fig. 3g compares the ratio of the area of the IR bands due to dimer and monomer for the free gas (at 2962 and 2903 cm^{-1}, respectively) and adsorbed phase (at 2946 and 2829 cm^{-1} respectively). In the gas phase, the ratio of dimer to monomer increases linearly with increasing pressure. However, the ratio of the dimer to monomer within the pores of MFM-300(Al) was constant across the pressure range studied. Moreover, this observation is consistent with the kinetic PXRD results (Fig. 3g), which show concurrent settlement of NO_2 and N_2O_4 molecules in the pore as a function of time. Thus, significantly, the equilibrium of the monomer-dimer ($2NO_2 \leftrightarrow N_2O_4$) transition is pressure-independent within the confined nano-voids of MFM-300(Al).

The presence of a single type of adsorbed NO_2 monomers, which are paramagnetic, is shown definitively by electron paramagnetic resonance (EPR) spectroscopy [Fig. 4a; bare MFM-300(Al) and N_2O_4 molecules at site II are

diamagnetic]. EPR spectra at 40 K show immobilised NO_2 with full resolution of the anisotropic electronic g-factor and ^{14}N hyperfine interaction[24]; at higher temperatures partial motion of the NO_2 is observed (Fig. S27). The interaction of NO_2 with the MOF interior is revealed by Davies ENDOR (electron nuclear double resonance) spectroscopy that resolves ^1H hyperfine interactions (Fig. 4b). Calculated spectra[25] confirm binding of NO_2 at site I, consistent with the end-on interaction with the –OH group and further interactions with the four adjacent aromatic -CH groups. Orientation selective ENDOR measurements show that the largest ^1H coupling to the –OH group is observed along the molecular NO_2 axis which is parallel to the O⋯O vector, further confirming the end-on binding unambiguously. Importantly, EPR data has also confirmed that electron transfer from NO_2 to the MOF does not occur, directly supporting the observed unusual reversibility of NO_2 uptake and hence the stability of the framework.

Our studies confirm that the interior of MFM-300(Al) can participate in weak additive, supramolecular interactions to stabilize the highly reactive NO_2 molecules with retention of its unpaired electron within the pore. A combination of these cooperative supramolecular interactions and spatial restriction within nanopores has enabled the unprecedented co-existence of NO_2 and N_2O_4 molecules and promoted the unusual stability of the extended $(NO_2 \cdot N_2O_4)_\infty$ chains within MFM-300(Al) as a crystalline matrix. The potential use of robust MOFs as viable solid sorbents for adsorptive removal of NO_2 could provide an exciting avenue to mitigate NO_x emissions.

References

1. Lelieveld, J. *et al.* Atmospheric oxidation capacity sustained by a tropical forest. *Nature* **452**, 737-740 (2008).
2. Edwards, P. M. *et al.* High winter ozone pollution from carbonyl photolysis in an oil and gas basin. *Nature* **514**, 351-354 (2014).
3. Chen, Z. Wang, J. Ma, G. Zhang, Y. China tackles the health effects of air pollution. *Lancet*, **382**, 1959-1960 (2013).
4. Feigin, V. L. *et al.* Global burden of stroke and risk factors in 188 countries, during 1990-2013: a systematic analysis for the global burden of disease study 2013. *Lancet Neurol.* **15**, 913-924 (2013).
5. Rezaei, F., Rownaghi, A. A., Monjezi, S., Lively, R. P. & Jones, C. W. SO_x/NO_x removal from flue gas streams by solid adsorbents: a review of current challenges and future directions. *Energy & Fuels* **29**, 5467-5486 (2015).
6. Goupil, J. M., Hemidy, J. F., Cornet, D. Adsorptin of NO_2 on modified Y zeolites. *Zeolites* **2**, 47-50 (1982).
7. Levasseur, B., Ebrahim, A. M. & Bandosz, T. J. Role of Zr^{4+} cations in NO_2 adsorption on $Ce_{1-x}Zr_xO_2$ mixed oxides at ambient conditions. *Langmuir* **27**, 9379-9386 (2011).
8. Levasseur, B., Ebrahim, A. M. & Bandosz, T. J. Interactions of NO_2 with amine-functionalized SBA-15: effects of synthesis route. *Langmuir* **28**, 5703-5714 (2012).
9. Florent, M., Tocci, M. & Bandosz, T. J. NO_2 adsorption at ambient temperature on urea-modified ordered mesoporous carbon. *Carbon* **63**, 283-293 (2013).
10. Belhachemi, M., Jeguirim, M., Limousy, L. & Addoun, F. Comparison of NO_2 removal using date pits activated carbon and modified commercialized activated carbon *via* different preparation methods: effect of porosity and surface chemistry. *Chem. Eng. J.* **253**, 121-129 (2014).
11. Zhou, H. C. and Kitagawa, S. Metal–organic frameworks (MOFs). *Chem. Soc. Rev.* **43**, 5415 (2014).
12. Yang, S. *et al.* Selectivity and direct visualization of carbon dioxide and sulfur dioxide in a decorated porous host. *Nat. Chem.* **4**, 887-894 (2012).

13. Ebrahim, A. M. & Bandosz, T. J. Effect of amine modification on the properties of zirconium–carboxylic acid based materials and their applications as NO_2 adsorbents at ambient conditions. *Microporous Mesoporous Mater.* **188**, 149-162 (2014).

14. Ebrahim, A. M., Levasseur, B. & Bandosz, T. J. Interactions of NO_2 with Zr-based MOF: effects of the size of organic linkers on NO_2 adsorption at ambient conditions. *Langmuir* **29**, 168-174 (2013).

15. Peterson, G. W., Mahle, J. J., DeCoste, J. B., Gordon, W. O. & Rossin, J. A. Extraordinary NO_2 removal by the metal–organic framework UiO-66-NH_2. *Angew. Chem. Int. Ed.* **55**, 6235-6238 (2016).

16. DeCoste, J. B., Demasky, T. J., Katz, M. J., Farha, O. K. & Hupp, J. T. A UiO-66 analogue with uncoordinated carboxylic acids for the broad-spectrum removal of toxic chemicals. *New J. Chem.* **39**, 2396-2399 (2015).

17. Ebrahim, A. M. & Bandosz, T. J. Ce(III) Doped Zr-based MOFs as excellent NO_2 adsorbents at ambient conditions. *ACS Appl. Mater. Interfaces* **5**, 10565-10573 (2013).

18. Levasseur, B., Petit, C. & Bandosz, T. J. Reactive adsorption of NO_2 on copper-based metal−organic framework and graphite oxide/metal−organic framework composites. *ACS Appl. Mater. Interfaces* **2**, 3606-3613 (2010).

19. Petit, C., Levasseur, B., Mendoza, B. & Bandosz, T. J. Reactive adsorption of acidic gases on MOF/graphite oxide composites. *Microporous Mesoporous Mater.* **154**, 107-112 (2012).

20. Kvick, Å., McMullan, R. K. & Newton, M. D. The structure of dinitrogen tetroxide N_2O_4: neutron diffraction study at 100, 60, and 20 K and *ab initio* theoretical calculations. *J. Chem. Phys.* **76**, 3754-3761 (1982).

21. Kachi-Terajima, C., Akatsuka, T., Kohbara, M.-a. & Takamizawa, S. Structural and magnetic study of N_2, NO, NO_2, and SO_2 adsorbed within a flexible single-crystal adsorbent of $[Rh_2(bza)_4(pyz)]_n$. *Chem. Asian J.* **2**, 40-50 (2007).

22. Wang, X., Hanson, J. C., Kwak, J. H., Szanyi, J. & Peden, C. H. F. Cation movements during dehydration and NO_2 desorption in a Ba–Y, FAU zeolite: an *in situ* time-resolved X-ray diffraction study. *J. Phys. Chem. C* **117**, 3915-3922 (2013).

23. Guttman, A. Absolute infrared intensity measurements on nitrogen dioxide and dinitrogen tetroxide. *J. Quant. Spectrosc. Radiat. Transfer* **2**, 1-15 (1962).

24. Shlotani, M. and Freed, J. H. ESR studies of NO_2 adsorbed on surfaces: analysis of motional dynamics. *J. Phys. Chem.* **85**, 3873-3883 (1981).

25. Stoll, S. and Schweiger, A. EasySpin, a comprehensive software package for spectral simulation and analysis in EPR. *J. Magn. Reson.* **178**, 42-55 (2006).

Methods

NO_2 safety: All systems involved in the supply, delivery and measurement of NO_2 were rigorously leak tested and used only within range of a NO_2 detection system with a sensitivity of 1 ppm. All gases exhausted from experimental apparatus was diluted with a flow of N_2 and fed into fume hood extracts.

Gas adsorption isotherms and breakthrough experiment: Measurements of NO_2 adsorption isotherm (0–1 bar) were performed using a Xemis gravimetric adsorption apparatus (Hiden Isochema, Warrington, UK) equipped with a clean ultrahigh vacuum system. The pressure in the system is accurately regulated by mass flow controllers. Research grade NO_2 and He were purchased from AIRLIQUIDE or BOC and used as received. In a typical gas adsorption experiment, 70-100 mg of MFM-300(Al)-solvate was loaded into the IGA, and degassed at 120 ºC and high dynamic vacuum (10^{-10} bar) for 1 day to give desolvated MFM-300(Al).

Breakthrough experiments were carried out in a 7 mm diameter fixed-bed tube of 120 mm length packed with ~3 g of MFM-300(Al) powder (particle size < 5 microns). The total volume of the bed was *ca.* 5 cm^3. The sample

was heated at 150 °C under a flow of He for 2 days for complete activation. The fixed bed was then cooled to room temperature (298 K) using a temperature programmed water bath and the breakthrough experiment was performed with a stream of 0.5% NO_2 (diluted in He and N_2) at atmospheric pressure and room temperature. The flow rate of the entering gas mixture was maintained at 40 mL min^{-1}, and the gas concentration, C, of NO_2 and N_2 at the outlet determined by mass spectrometry and compared with the corresponding inlet concentration C_0, where $C/C_0 = 1$ indicates complete breakthrough. A more detailed description is given in SI.

High resolution synchrotron X-ray powder diffraction and structure determinations: High resolution *in situ* synchrotron X-ray powder diffraction (PXRD) data were collected at Beamline ID22 of European Synchrotron Radiation Facility (ESRF) using monochromated radiation [λ = 0.399999(2) Å]. These *in situ* diffraction measurements were carried out in capillary mode and the temperature controlled by an Oxford Cryosystems open-flow N_2 gas cryostat. In a typical experiment, the powder sample of MFM-300(Al) (~2 mg) was dried in air and ground for 10 mins before loading into a capillary tube (0.7 mm diameter). Grinding provides a uniform and small (below 10 micron) particle size essential for obtaining high-quality X-ray patterns. The capillary tube was connected to high vacuum (10^{-6} mbar) and heated at 150 °C for ~4 h to generate desolvated MFM-300(Al). Upon loading of NO_2 into MFM-300(Al) at 1 bar and 298 K, a series of rapid scans (~10 mins each) were collected to capture the changes in the unit cell parameters as a function of time. Longer scans (~20 mins each) were collected when reaching the adsorption equilibrium at 298 K. A PXRD pattern was also collected after a final degassing under heating for ~1h to remove adsorbed NO_2 molecules. A second cycle of NO_2 adsorption/desorption was also carried out to test the structural stability and durability of this MOF material. Upon desolvation and NO_2 loading, we observe neither changes to cell parameters nor additional/missing features in the patterns, suggesting that there is no structural phase change during the experiment.

The structure solutions were initially established by considering the structure of bare MFM-300(Al) framework, and the residual electron density maps were further developed from subsequent difference Fourier analysis using TOPAS. Lattice parameters were obtained from *Le Bail* refinements of the PXRD data. The final structure refinement of MFM-300(Al)·$(NO_2)_2$·$(N_2O_4)_2$ was carried out using the Rietveld method with isotropic displacement parameters for all atoms. Upon the NO_2 loading, there are apparent changes in intensities of the Bragg peak indicating that the NO_2 molecules are adsorbed into the material. NO_2 and N_2O_4 molecules at each site were determined to be nearly fully occupied, in excellent agreement with the experimental isotherm value. The final stage of the Rietveld refinement involved soft restraints to the C-C bond lengths within the benzene rings. Rigid body refinement was applied to the NO_2 and N_2O_4 molecules in the pore.

Crystal data for MFM-300(Al)·$(NO_2)_2$·$(N_2O_4)_2$: [$Al_2(OH)_2(C_{16}H_6O_8)$]·$(NO_2)_2$·$(N_2O_4)_2$. Yellow powder. Tetragonal, space group $I4_122$, $a = b = 14.84158(5)$, $c = 11.81181(5)$ Å, $V = 2601.82(2)$ Å^3, $M = 690.23$, $T = 298(2)$ K, $Z = 4$. The

final Rietveld plot corresponds to satisfactory crystal structure model (R_{Bragg} = 0.018) and profile (R_p = 0.043 and R_{wp} = 0.058) indicators with a goodness-of-fit parameter of 1.750.

Supplementary Information is available in the online version of the paper.

Author Contributions SY, HGWG, XH and LB: syntheses, characterisation of MOF samples, measurements of adsorption isotherms and breakthrough data. KMT: analysis of isotherms. SY, JS and CD: collection and analysis of synchrotron X-ray powder diffraction data. SY, YC, LLD and AJRC: collection and analysis of neutron scattering data. AJD and MWG: collection and analysis of IR data. XH, AMS, FT and EJLM: collection and analysis of EPR data. SY and MS: overall direction of project and preparation of the manuscript.

Author Information The crystal structure of MFM-300(Al)·(NO$_2$)$_2$·(N$_2$O$_4$)$_2$ is available free of charge from the Cambridge Crystallographic Data Centre under reference number CCDC-1539036. Reprints and permissions information is available at www.nature.com/reprints. The authors declare no competing financial interests. Correspondence and requests for materials should be addressed to S.Y. (Sihai.Yang@manchester.ac.uk) and M.S. (M.Schroder@manchester.ac.uk).

Competing financial interests The authors declare no competing financial interests.

Data availability. All relevant data are available from the authors, and/or are included with the manuscript.

Figures and Legends

a

b

c

d

e

f
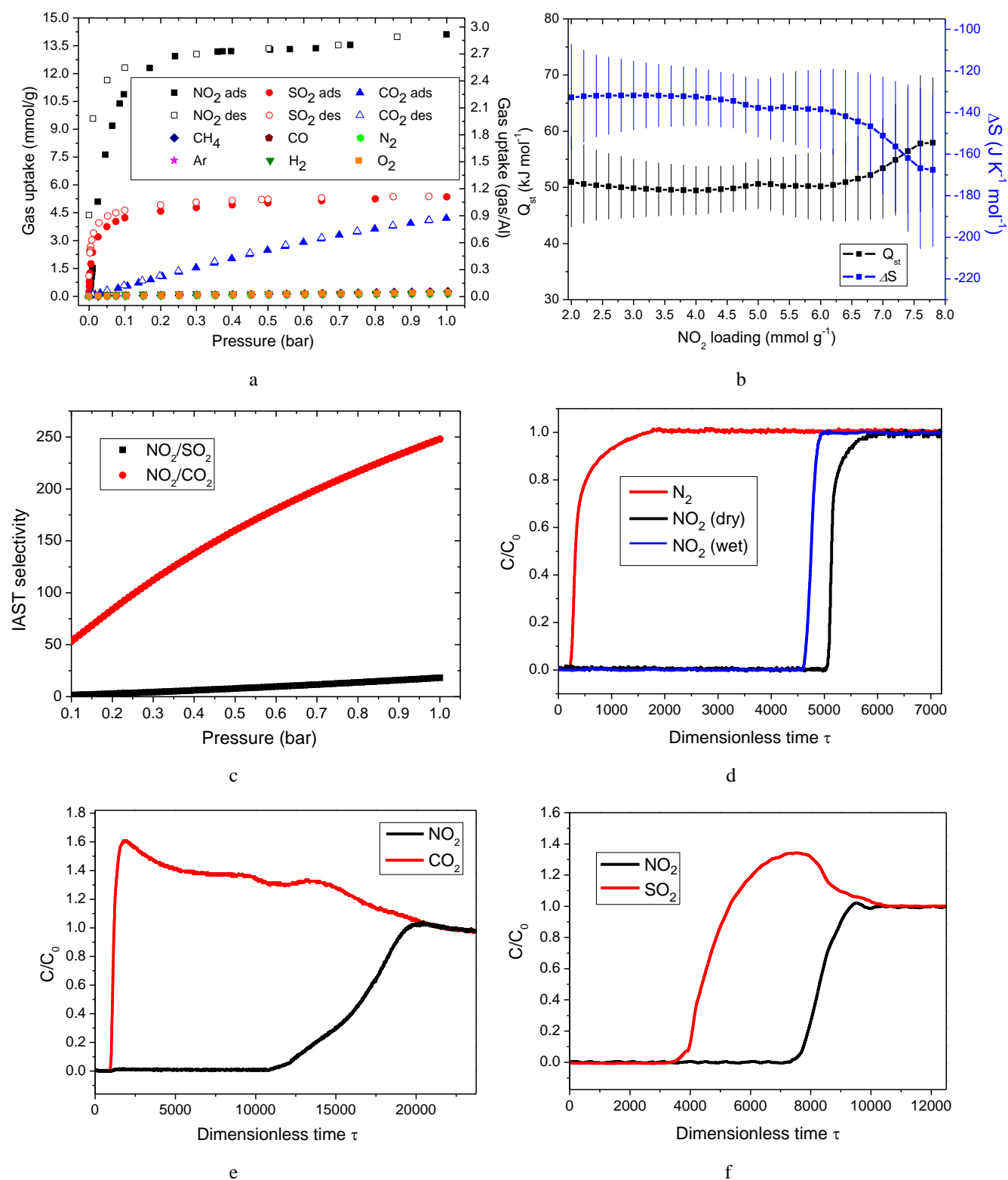
Figure 1. NO₂ adsorption, thermodynamics, selectivity and breakthrough data in MFM-300(Al). (a) Adsorption isotherms of NO_2, SO_2, CO_2, CH_4, N_2, CO, H_2, O_2 and Ar in MFM-300(Al) at 298 K. (b) Variation of the thermodynamic parameters of isosteric heat of adsorption (Q_{st}) and entropy (ΔS) for NO_2 uptakes in MFM-300(Al). Overall, ΔS decreases slowly with increasing surface coverage. (c) Comparison of IAST selectivities for equimolar mixtures of NO_2/SO_2 and NO_2/CO_2 (NO_2/N_2 data shown in SI) at 0.1-1.0 bar for MFM-300(Al) at 298 K. IAST calculations at low pressure (<0.1 bar) carries very large uncertainties due to the insufficient integration of spreading pressure and are thus not reported. (d) Dimensionless breakthrough curve of 0.5% NO_2 (5000 ppm) diluted in He/N_2 under both dry and wet conditions in a fixed-bed packed with MFM-300(Al) at 298 K and 1 bar. (e) Dimensionless breakthrough curve of 0.4% NO_2 (4000 ppm) and 15% CO_2 (v/v) diluted in He in a fixed-bed packed with MFM-300(Al) at 298 K and 1 bar. (f) Dimensionless breakthrough curve of 0.16% NO_2 (1666 ppm) and 0.34% SO_2 (3334 ppm) diluted in He in a fixed-bed packed with MFM-300(Al) at 298 K and 1 bar.
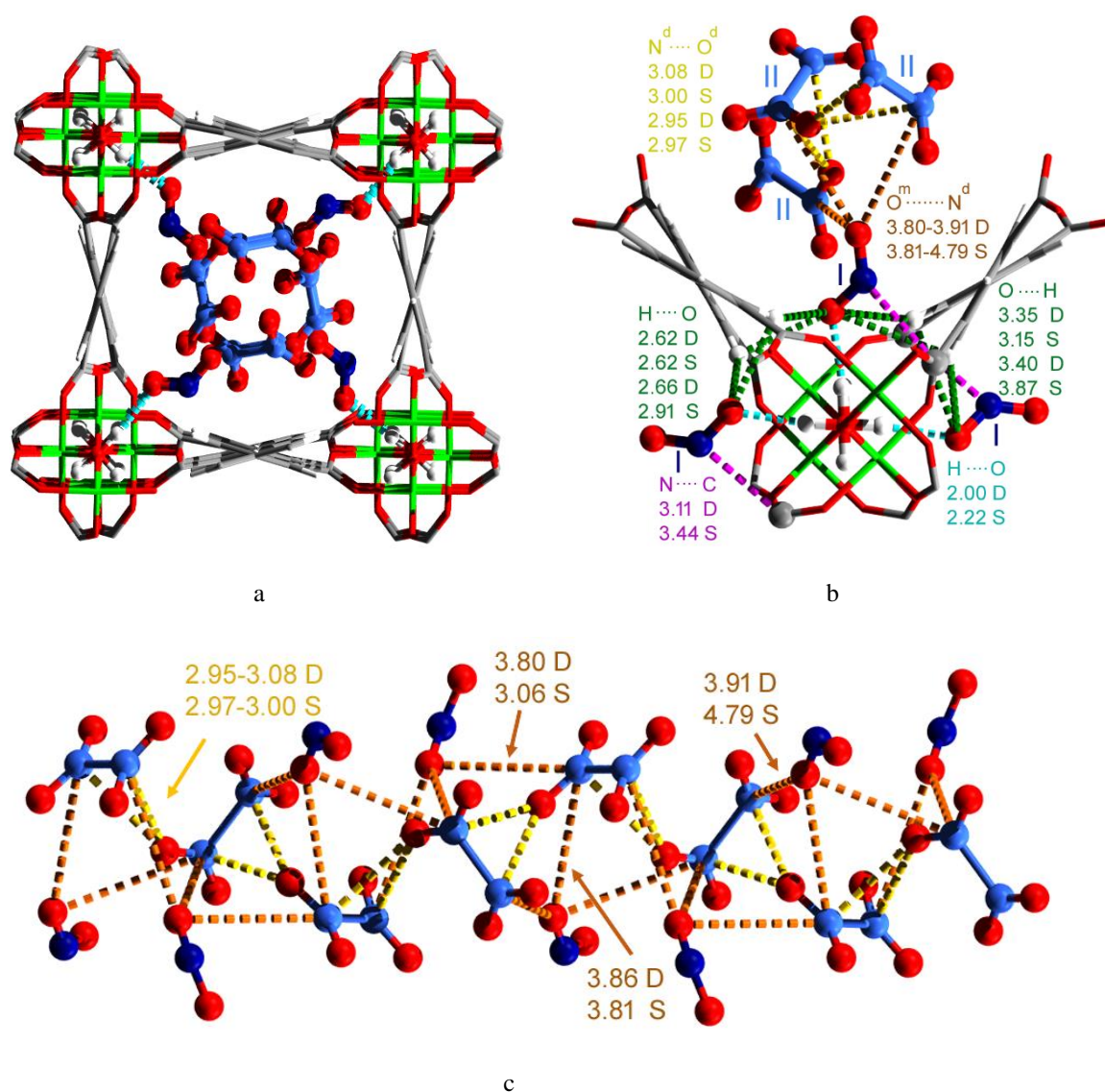
Figure 2. Views of the structural model for MFM-300(Al)·(NO₂)₂·(N₂O₄)₂ determined by high resolution synchrotron X-ray powder diffraction data at 298 K and DFT calculations (Al: green; carbon: grey; oxygen: red; hydrogen: white; nitrogen: blue). The structural model was first obtained by Rietveld refinement of the PXRD data and subsequently optimised by DFT calculations to simplify the positional disorder of adsorbed gas molecules owing to their thermal motion. (a),(b) Host-guest binding details showing the binding sites I and II. (c) Structural view of the one-dimensional helical chain $(NO_2 \cdot N_2O_4)_\infty$ within the channel of MFM-300(Al). The O···HO hydrogen-bonds, C···N dipole, H···O supramolecular interactions, and inter-molecular dipole interactions ($O^m \cdots N^d$ and $N^d \cdots O^d$, where m and d represents for monomer and dimer, respectively) are highlighted in cyan, purple, green, orange and yellow, respectively. The nitrogen atoms of NO_2 and N_2O_4 are highlighted in deep and light blue, respectively. The bond distances, quoted in Å, obtained from DFT calculations and synchrotron X-ray diffraction are labelled as D and S, respectively, and show excellent agreement. Throughout this report, the uncertainties for the bond distance obtained from synchrotron X-ray diffraction are below 0.01 Å. In X-ray diffraction experiments, disorder of molecules was observed owing not only to thermal motion, but also to the nature of the soft binding to these molecules within the pore. For clarity, the average positions of disordered molecules are shown here and disordered models are shown in SI.
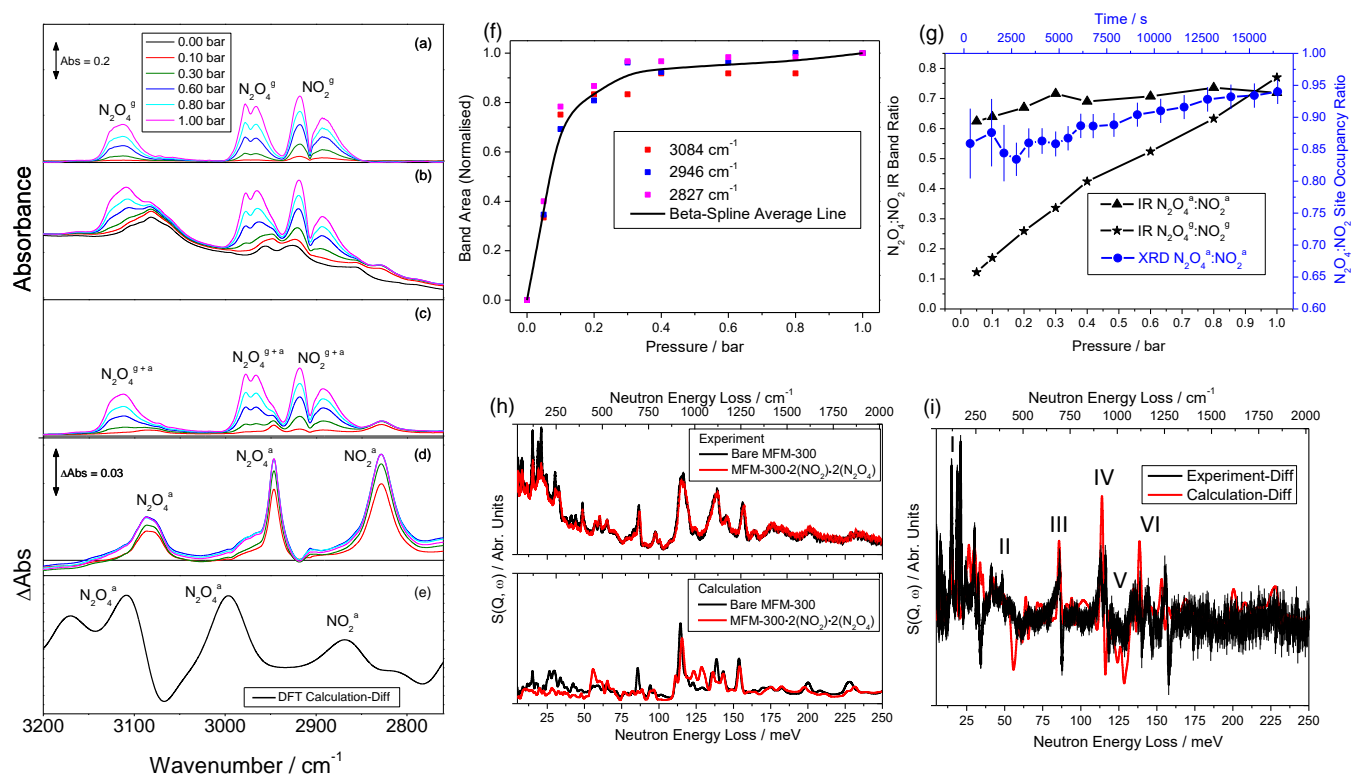
Figure 3. Fourier transform infrared spectroscopy (FTIR) and inelastic neutron scattering (INS) spectra for MFM-300(Al) as a function of NO₂ loading. No abscissa scale factor was used throughout this report for IR and INS calculations. *In situ* FTIR spectra of gaseous and/or adsorbed NO_2 and N_2O_4 molecules between 0.00 - 1.00 bar at 298 K in samples of (a) KBr, (b) KBr + MFM-300(Al) (KBr background), (c) KBr + MFM-300(Al) [KBr + MFM-300(Al)-0.00 bar background] and (d) the difference spectra showing the growth of three new bands in the overtone region due to adsorbed NO_2 and N_2O_4 molecules in the pore. (e) DFT simulated difference IR spectra for adsorbed NO_2 and N_2O_4 molecules in the pore of MFM-300(Al), showing the growth of four new bands at the overtone region, in excellent agreement with the experimental data shown in (d). The overtone bands were calculated using a scale factor of 2.00. (f) Comparison of the variation of band areas of the three new bands (normalised to 1 at 1.00 bar) with pressure for the uptake of NO_2 and N_2O_4 into MFM-300(Al). (g) Ratio of the IR bands of dimer and monomer species of NO_2 adsorbed in MFM-300(Al) (labelled as $N_2O_4^a$ and NO_2^a) and in the free gas phase (labelled as $N_2O_4^g$ and NO_2^g), showing that in the gas phase the dimer increases relative to monomer as the pressure is increased, whereas in the pores it is constant. For comparison, the ratio of the refined site occupancies for adsorbed N_2O_4 and NO_2 molecules from the PXRD study is also included. It is worth noting that the conversion of the ratio of the IR band areas to the absolute site occupancies is subject to a factor of the extinction coefficient of the dimer/monomer. (h) Comparison of the experimental (top) and DFT simulated (bottom) of INS spectra for bare and the NO_2-loaded MFM-300(Al). (i) Comparison of the difference plots for experimental and DFT calculated INS spectra of bare and the NO_2-loaded MFM-300(Al).
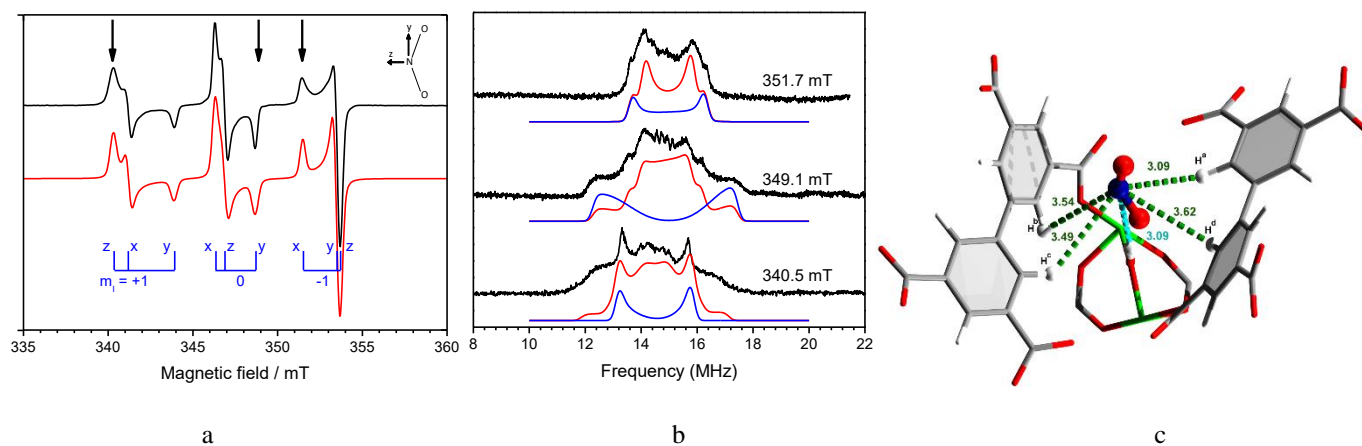
Figure 4. EPR and ^{1}H ENDOR spectra of MFM-300(Al)·(NO$_2$)$_2$·(N$_2$O$_4$)$_2$. (a) Continuous wave (cw) X-band (9.72 GHz) EPR spectrum at 40 K (black) and simulation (red) with g_x = 2.0052, g_y = 1.9915, g_z = 2.0021 and ^{14}N nuclear hyperfine interactions (nuclear spin, I = 1) of A_x = 144, A_y = 135, A_x = 185 MHz, where x, y and z define the NO$_2$ molecular axes (inset). NO$_2$ has C$_{2v}$ point symmetry with the z-axis along the C$_2$ rotation axis, y parallel to the O…O vector, and x normal to the NO$_2$ plane. The hyperfine interactions are much larger than the g-anisotropy such that the transitions are grouped according to the m_I value as shown by the stick spectrum. This allows orientation selection in the ENDOR studies by choice of the static magnetic field. The cw EPR simulation also includes unresolved ^{1}H hyperfine couplings (I = ½) determined from the ENDOR study; this gives a better fit to the experimental line-shapes. (b) X-band Davies ENDOR spectrum (black) at 40 K and the static magnetic fields indicated, shown by the arrows in (a), dominantly selecting the NO$_2$ x, y and z-axes (top-to-bottom), respectively. ENDOR gives pairs of transitions separated by the effective hyperfine coupling for the orientations selected, centred on the Larmor frequency of the nucleus being probed (14.9 MHz for ^{1}H at 350 mT). The red and blue lines are calculated spectra, using a simple dipolar model derived from the DFT-optimised NO$_2$ and H coordinates, as shown in (c). The red spectrum includes the –OH group and four aromatic –CH groups (all other ^{1}H nuclei lie much further from the NO$_2$). The blue spectrum includes only the –OH group, showing that the strongest coupling to this ^{1}H is found approximately along the NO$_2$ y-axis (the <u>N</u>O$_2$…O<u>H</u> vector lies at 159° to the NO$_2$ y-axis). Full details of the model are given in SI.

Supplementary Information

Index of Supplementary Information

1.   Experimental Section

1.1   Synthesis and Activation of MFM-300(Al)

All reagents were used as received from commercial suppliers without further purification. Synthesis of [$Al_2(OH)_2(C_{16}O_8H_6)$]($H_2O)_6$ [MFM-300(Al)-solvate] and activation of [$Al_2(OH)_2(C_{16}O_8H_6)$] [MFM-300(Al)] were carried out using our previously reported method.[1]

1.2   NO$_2$ Safety

All systems involved in the supply, delivery and measurement of NO$_2$ were rigorously leak tested and used only within range of a NO$_2$ detection system with a sensitivity of 1 ppm. All gases exhausted from experimental apparatus was diluted with a flow of N$_2$ and fed into fume hood extracts.

1.3   Gas Adsorption Isotherms and Breakthrough Experiment

Measurements of NO$_2$ adsorption isotherm (0–1 bar) were performed using a Xemis gravimetric adsorption apparatus (Hiden Isochema, Warrington, UK) equipped with a clean ultrahigh vacuum system. The pressure in the system is accurately regulated by mass flow controllers. Research grade NO$_2$ and He were purchased from AIRLIQUIDE or BOC and used as received. In a typical gas adsorption experiment, 70-100 mg of MFM-300(Al)-solvate was loaded into the Xemis, and degassed at 120 $^{\circ}$C and high dynamic vacuum (10^{-10} bar) for 1 day to give desolvated MFM-300(Al).

Breakthrough experiments were carried out in a 7 mm diameter fixed-bed tube of 120 mm length packed with ~3 g of MFM-300(Al) powder (particle size < 5 microns). The total volume of the bed was *ca.* 5 cm^3. The sample was heated at 150 $^{\circ}$C under a flow of He for 2 days for complete activation. The fixed bed was then cooled to room temperature (298 K) using a temperature programmed water bath and the breakthrough experiment was performed with a stream of 0.5% NO$_2$ (diluted in He and N$_2$ under both dry and wet conditions) at atmospheric pressure and room temperature. The flow rate of the entering gas mixture was maintained at 40 mL min^{-1}, and the gas concentration, *C*, of NO$_2$ and N$_2$ at the outlet determined by mass spectrometry and compared with the corresponding inlet concentration C_0, where $C/C_0 = 1$ indicates complete breakthrough. Breakthrough separation of NO$_2$/CO$_2$ was conducted using a mixture containing 0.4% NO$_2$ (4000 ppm) and 15% CO$_2$ (v/v) diluted in He in a fixed-bed packed with MFM-300(Al) at 298 K and 1 bar at a flow rate of 47 mL min^{-1}. Breakthrough separation of NO$_2$/SO$_2$ was conducted using a mixture containing 0.16% NO$_2$ (1666 ppm) and 0.34% SO$_2$ (3334 ppm) diluted in He in a fixed-bed packed with MFM-300(Al) at 298 K and 1 bar at a flow rate of 19 mL min^{-1}. The final results have been converted to dimensionless plots as shown in Figure 1.

1.4   *In situ* FTIR Spectroscopy

In situ studies of MFM-300(Al) were carried out in a high-pressure low temperature cell, which has been described in detail elsewhere.[2] A KBr disc with and without MFM-300(Al) (*ca.* 5 wt%) was used as the matrix for *in situ* IR experiments to record the spectra for the material and background (*i.e.,* gaseous phase NO_2), respectively. MFM-300(Al) was pressed into the surface of a preformed KBr disc. The discs were further degassed by heating to 120 °C under high vacuum overnight and mounted into the cell, which was purged with Ar. The disc was placed under vacuum, cooled to 298 K and filled to various pressures between 0 and 1 bar of NO_2 (CP grade, supplied by AIRLIQUIDE) to mimic gas sorption experiments. For each pressure step, the equilibration time was set to 120 min before the measurement of IR spectra. All IR spectra were recorded on a Nicolet Avatar 360 FTIR spectrometer with a liquid N_2 cooled HgCdTe detector. Throughout this report, intensities of the overtone bands were used for analysis because these bands had a lower absorption than the fundamental bands for the monomer and dimer, both of which had an absorbance greater than 1 at pressures over 0.3 bar in our apparatus. A low spectral resolution (2 cm^{-1}) was used to allow for efficient subtraction of the bands due to the free gas.

1.5   Inelastic Neutron Scattering (INS)

INS spectra were recorded on the VISION spectrometer at Spallation Neutron Source, Oak Ridge National Laboratory (USA). VISION is an indirect geometry crystal analyser instrument that provides a wide dynamic range with high resolution. The sample of desolvated MFM-300(Al) was loaded into a cylindrical vanadium sample container with an indium vacuum seal and connected to a gas handling system. The sample was degassed at 10^{-7} mbar at 120 °C for 1 day to remove any remaining trace guest water molecules. The temperature during data collection was controlled using a closed cycle refrigerator (CCR) cryostat (10 ± 0.1 K). The loading of NO_2 was performed volumetrically at room temperature in order to ensure that NO_2 was present in the gas phase when not adsorbed and also to ensure sufficient mobility of NO_2 inside the crystalline structure of MFM-300(Al). Subsequently, the temperature was reduced to below 10 K in order to perform the scattering measurements with the minimum achievable thermal motion for the framework host and adsorbed NO_2 and N_2O_4 molecules. Background spectra [sample can plus bare MFM-300(Al)] were subtracted to obtain the difference spectra.

INS was used to study the binding interaction and structure dynamics in this case because it has several unique advantages:

•   INS spectroscopy is ultra-sensitive to the vibrations of hydrogen atoms, and hydrogen is ten times more visible than other elements due to its high neutron cross-section.

•   The technique is not subject to any optical selection rules. All vibrations are active and, in principle, measurable.

- INS observations are not restricted to the centre of the Brillouin zone (gamma point) as is the case for optical techniques.

- INS spectra can be readily and accurately modelled: the intensities are proportional to the concentration of elements in the sample and their cross-sections, and the measured INS intensities relate straightforwardly to the associated displacements of the scattering atom. Treatment of background correction is also straightforward.

- Neutrons penetrate deeply into materials and pass readily through the walls of metal containers making neutrons ideal to measure bulk properties of this material.

- INS spectrometers cover the whole range of the molecular vibrational spectrum, 0-500 meV (0-4000 cm^{-1})

- INS data can be collected at below 10 K, where the thermal motion of the MOF material and adsorbed NO_2, and N_2O_4 molecules can be significantly reduced.

- Calculation of the INS spectra by DFT vibrational analysis can be readily achieved, and DFT calculations relate directly to the INS spectra, and, in the case of solid state calculations, there are no approximations other than the use of DFT eigenvectors and eigenvalues to determine the spectral intensities.

1.6 DFT Calculations and Molecular Dynamic Modelling

The vibrational properties of the bare and NO_2-loaded MFM-300(Al) were calculated using a combination of density functional theory (DFT) and plane-wave pseudopotential methods as implemented in the CASTEP code,[3] using ultra-soft pseudopotentials with a plane-wave energy cut-off of 380 eV. Calculations were performed under the PBE approximation[3] for exchange and correlation. The electronic structure was calculated on a 2×2×2 Monkhorst-Pack mesh for the unit cell (see crystal data in Section 1.7). The normal modes of the solid were determined from dynamical matrices calculated using finite displacements, by numerical differentiation, and the lattice parameters and atomic coordinates determined by PXRD in this work were used for the initial structure. The total energy tolerance for electronic energy minimization was 5×10^{-10} eV/atom, and 5×10^{-9} eV/atom for structure optimization. The maximum interatomic force after relaxation was below 0.001 eV/Å. The INS spectra were the calculated using the aClimax software,[4] and IR spectra calculated using CASTEP.[3] The information was used to identify the modes of vibrational features in the experimental INS and FTIR spectra, and no abscissa scale factor was used throughout this report for INS or IR calculations. The calculated INS spectrum shows the total transitions (up to 10 orders). The stepwise calculation for binding energies was carried out by (i) optimising the structure of the bare MOF by finding the local potential energy minimum with the final potential energy E_1; (ii) optimising the structure of the NO_2-loaded MOF (3 NO_2/Al) with the final potential energy E_2; (iii) removing the MOF host, leaving the NO_2 and N_2O_4 (ratio of 1: 1) molecules in the system, enlarging the unit cell to 2.5x2.5x2.5 nm^3 and redistributing the NO_2 and N_2O_4 molecules randomly to afford a reminiscent of gas phase interaction in the three dimensional space to minimize the energy E_3.

The NO_2 binding energy (ΔE) was obtained by the calculation of $\Delta E = E_1 - E_2 + E_3$. MD modelling at 600K was carried out by CASTEP[3], with a timestep of 1fs and a total of 10000 steps under NVT ensemble (controlled by Hoover-Langevin thermostat). For the MD simulation, the electronic structure was calculated on gamma-point only, and the tolerance for electronic energy minimization was 5×10^{-6} eV/atom. The purpose of the MD modelling is to study the stability of the $(NO_2 \cdot N_2O_4)_\infty$ chain due to the confinement within the pores, by comparing the molecular dynamics with and without the MOF. Indeed, within the simulation timescale of 10ps, the $(NO_2 \cdot N_2O_4)_\infty$ chain shows exceptional stability at room temperature in MD modelling and even at elevated temperature of 600 K. The MD calculation was terminated at 600 K where the MOF host starts to show thermal decomposition in reality. It is worth noting that this result is subject to various limitations of the MD modelling, particularly for the limited timescale in MD when comparing with the laboratory timescale of seconds or longer. In this case, it demonstrates the role of the MOF in stabilising the $(NO_2 \cdot N_2O_4)_\infty$ chain from a theoretical perspective.

1.7 High Resolution Synchrotron X-ray Powder Diffraction and Structure Determinations

High resolution *in situ* synchrotron X-ray powder diffraction (PXRD) data were collected at Beamline ID22 of European Synchrotron Radiation Facility (ESRF) using monochromated radiation [$\lambda = 0.399999(2)$ Å]. These *in situ* diffraction measurements were carried out in capillary mode and the temperature controlled by an Oxford Cryosystems open-flow N_2 gas cryostat. In a typical experiment, the powder sample of MFM-300(Al) (~2 mg) was dried in air and ground for 10 mins before loading into a capillary tube (0.7 mm diameter). Grinding provides a uniform and small (below 10 micron) particle size essential for obtaining high-quality X-ray patterns. The capillary tube was connected to high vacuum (10^{-6} mbar) and heated at 150 °C for ~4 h to generate desolvated MFM-300(Al). Upon loading of NO_2 into MFM-300(Al) at 1 bar and 298 K, a series of rapid scans (~10 mins each) were collected to capture the changes in the unit cell parameters as a function of time. Longer scans (~20 mins each) were collected when reaching the adsorption equilibrium at 298 K. A PXRD pattern was also collected after a final degassing under heating for ~1h to remove adsorbed NO_2 molecules. A second cycle of NO_2 adsorption/desorption was also carried out to test the structural stability and durability of this MOF material. Upon desolvation and NO_2 loading, we observe neither changes to cell parameters nor additional/missing features in the patterns, suggesting that there is no structural phase change during the experiment.

The structure solutions were initially established by considering the structure of bare MFM-300(Al) framework, and the residual electron density maps were further developed from subsequent difference Fourier analysis using TOPAS.[5] Lattice parameters were obtained from *Le Bail* refinements of the PXRD data. The final structure refinement of MFM-300(Al)·$(NO_2)_2$·$(N_2O_4)_2$ was carried out using the Rietveld method with isotropic displacement parameters for all atoms. Upon the NO_2 loading, there are apparent changes in intensities of the Bragg

peak indicating that the NO_2 molecules are adsorbed into the material. NO_2 and N_2O_4 molecules at each site were determined to be nearly fully occupied, in excellent agreement with the experimental isotherm value. The final stage of the Rietveld refinement involved soft restraints to the C-C bond lengths within the benzene rings. Rigid body refinement was applied to the NO_2 and N_2O_4 molecules in the pore.

Crystal data for MFM-300(Al)·(NO_2)₂·(N_2O_4)₂: [$Al_2(OH)_2(C_{16}H_6O_8)$]·(NO_2)₂·(N_2O_4)₂. Yellow powder. Tetragonal, space group $I4_122$, $a = b = 14.84158(5)$, $c = 11.81181(5)$ Å, $V = 2601.82(2)$ Å³, $M = 690.23$, $T = 298(2)$ K, $Z = 4$. The final Rietveld plot corresponds to satisfactory crystal structure model ($R_{Bragg} = 0.018$) and profile ($R_p = 0.043$ and $R_{wp} = 0.058$) indicators with a goodness-of-fit parameter of 1.750. CCDC deposition number: 1539036. Final fractional coordinates and bond distances for MFM-300(Al)·(NO_2)₂·(N_2O_4)₂ are listed in Table S1 and S2, respectively.

Table S1. List of atomic positions for MFM-300(Al)·(NO_2)₂·(N_2O_4)₂.

	Site-num	x	y	z	B_{iso} (Å²)
Al1	8	1.30586(10)	-0.30586(10)	0.5	3.894(67)
O1	8	0.75170(26)	0.25	0.625	3.762(63)
O2	16	0.87600(18)	0.12440(20)	1.10416(21)	3.762(63)
O3	16	0.89443(17)	0.21604(17)	0.25359(28)	3.762(63)
C1	16	0.86199(29)	0.09141(30)	0.79768(38)	4.095(82)
C2	16	0.54435(20)	0.43176(12)	0.76209(19)	4.095(82)
C3	8	0.5	0.5	0.70087(26)	4.095(82)
C4	16	0.53865(21)	0.42815(11)	0.87983(14)	4.095(82)
C5	8	0.5	0.5	0.93826(21)	4.095(82)
H1	8	0.80864	0.25	0.625	5.643(95)
H2	8	0.5	0.5	0.61237	4.914(99)
H3	16	0.56718	0.37862	0.90735	4.914(99)
N2	16	0.01401903	0.2414441	-0.484625	30.9(18)
O3s	16	-0.05095469	0.2485398	-0.4407144	12.50(43)
O4s	16	0.06229106	0.2334176	-0.4146818	18.49(72)
N3	16	0.1872874	0.3562286	-0.6306682	37.75(60)
O3a	16	0.2488465	0.3868339	-0.5745081	37.75(60)
O3b	16	0.1792254	0.3776048	-0.7296211	37.75(60)
N4	16	0.1236334	0.2941813	-0.5797326	37.75(60)
O4a	16	0.06221788	0.2633852	-0.6359762	37.75(60)
O4b	16	0.131767	0.2727097	-0.4808217	37.75(60)

Table S2. List of bond lengths for MFM-300(Al)·(NO_2)₂·(N_2O_4)₂.

Bond	Distance (Å)	Bond	Distance (Å)
Al1-O1	1.8967(22)	C2-C3	1.4078(27)
Al1-O2	1.9153(32)	C2-C4	1.3943(29)
Al1-O3	1.8727(25)	C4-C5	1.3937(24)
C1-O2	1.2725(50)	C5-C5	1.4586(49)
C1-O3	1.3236(52)		
C1-C2	1.4347(50)		

1.8   EPR Measurements

Continuous wave (cw) and pulsed electron paramagnetic resonance (EPR) measurements of powder samples of the bare and NO_2-loaded MFM-300(Al) were performed at X-band (*ca.* 9.7 GHz) on a Bruker Elexsys E580 spectrometer. The microwave frequency was measured with a built-in digital counter and the magnetic field was calibrated using a Bruker strong pitch reference sample. A modulation amplitude of 0.1 mT and microwave powers of 0.002-2 mW were used. Electron-nuclear double resonance (ENDOR) measurements used the Davies sequence[6] ($\pi_{inv} - RF - \pi/2 - \tau - \pi - \tau - echo$) with microwave inversion and radiofrequency (RF) π-pulse durations of 200 and 1800 ns, respectively. EPR and ENDOR spectra were calculated using the EasySpin toolbox for Matlab.[7,8]

2.   *In Situ* Synchrotron X-Ray Powder Diffraction Patterns

The adsorption, diffusion and binding domains for NO_2 within MFM-300(Al) were studied by *in situ* high resolution synchrotron X-ray powder diffraction (PXRD) experiments. Desolvated MFM-300(Al) shows negligible residual electron density in the void. Upon loading NO_2 at 1 bar at 298 K, high resolution PXRD data (approximately 600-1200s for each scan) were collected over a period of 5h to monitor diffusion of molecules into MFM-300(Al). Initially, a steady exponential increase in the *a*-axis and cell volume of MFM-300(Al) was observed, indicating diffusion of NO_2 molecules within MFM-300(Al) (Figs. S6-S7). After 2h, further changes in the cell parameters were negligible, indicating the formation of an equilibrated host-guest structure. The PXRD data between 2-5 h were merged to improve the signal-to-noise ratio for determination of locations of adsorbed NO_2 molecules *via* Rietveld refinement. Comparison of the PXRD patterns for the bare and NO_2-loaded MOF shows retention of the crystal structure and significant variations in the peak intensities as a result of NO_2 binding (Fig. S3). Analysis of the Fourier density map revealed two independent binding sites (I and II) within the pore of MFM-300(Al). According to the shape and height of the peaks, sites I and II were assigned as NO_2 and N_2O_4 molecules, respectively, and a highly satisfactory Rietveld refinement was obtained (Fig. S4). To confirm further the model, DFT calculations were used to optimize the structures for bare MFM-300(Al) and MFM-300(Al)·$(NO_2)_2$·$(N_2O_4)_2$. Initially, the structural models obtained from synchrotron PXRD experiments were adapted into the calculations. Upon convergence, excellent agreement between calculated and experimental models for the structure was obtained. The bond distances obtained by independent analysis of PXRD and DFT calculations are compared in Fig. 2 with excellent agreement between the two. The binding energy of NO_2 in MFM-300(Al) has also been obtained by DFT calculations at a loading of 14.5 mmol g^{-1} (equivalent to $3NO_2$/Al), to be 44 kJ mol^{-1}.
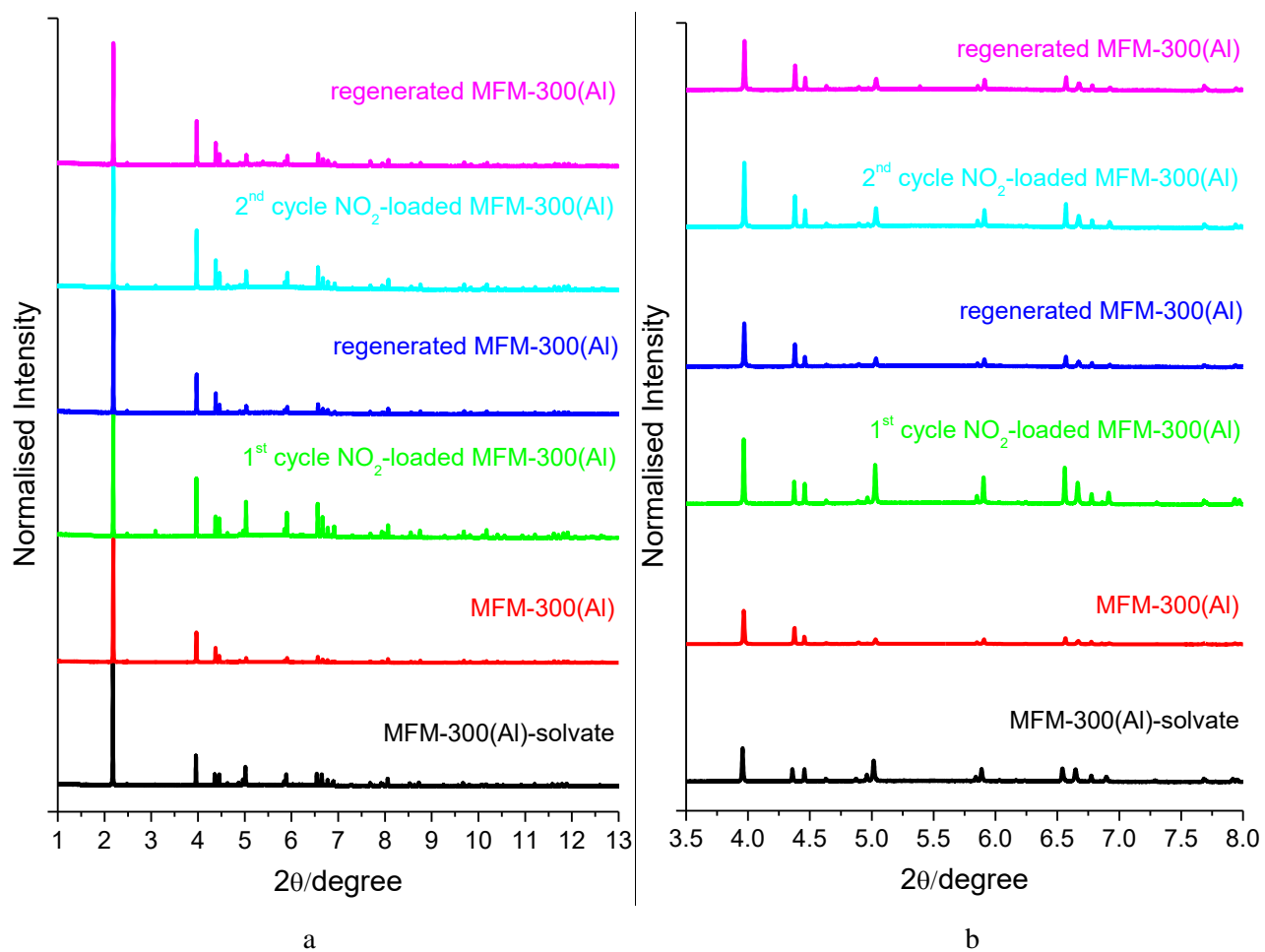
Figure S1. (a) Powder X-ray diffraction patterns for solvated, desolvated, NO_2-loaded, and regenerated MFM-300(Al) samples for two cycles of NO_2 adsorption/desorption at 298 K [$\lambda = 0.399999(2)$ Å]; (b) higher angle data ($2\theta = 3.5-8°$) has been scaled up confirming that MFM-300(Al) retains high crystallinity on cyclic uptake/removal of NO_2.

NO$_2$ sorption cycle 5

NO$_2$ sorption cycle 4

NO$_2$ sorption cycle 3

NO$_2$ sorption cycle 2

NO$_2$ sorption cycle 1

MFM-300(Al)

Normalised Intensity

2θ/degrees
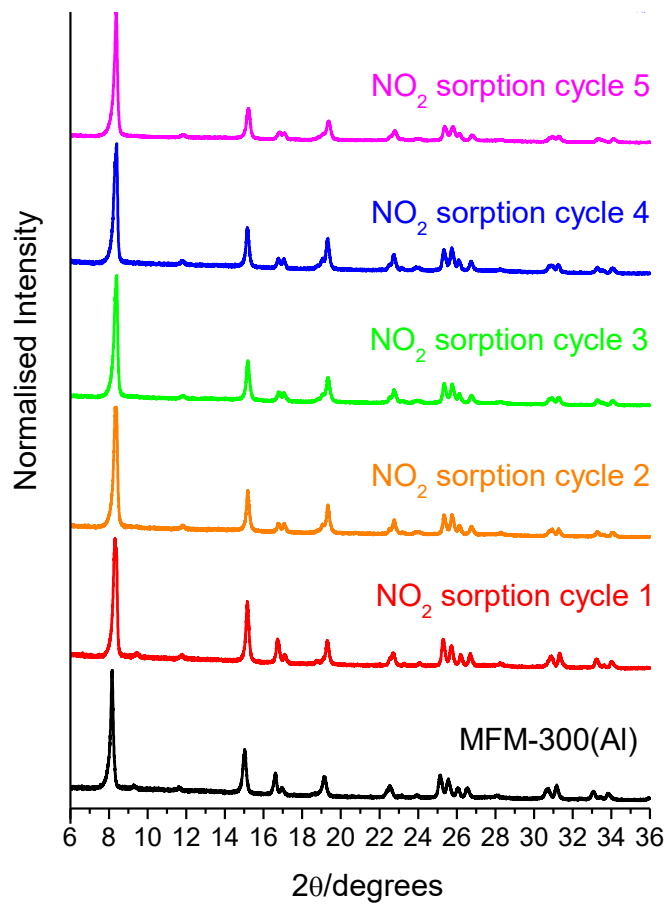
a   b [to be added]

Figure S2. (a) Powder X-ray diffraction patterns for MFM-300(Al) samples upon adsorption/desorption cycle of NO$_2$ for five cycles at 298 K [λ = 1.54056(2) Å]; (b) comparison of the NO$_2$ uptake capacities over five cycles at 298 K.
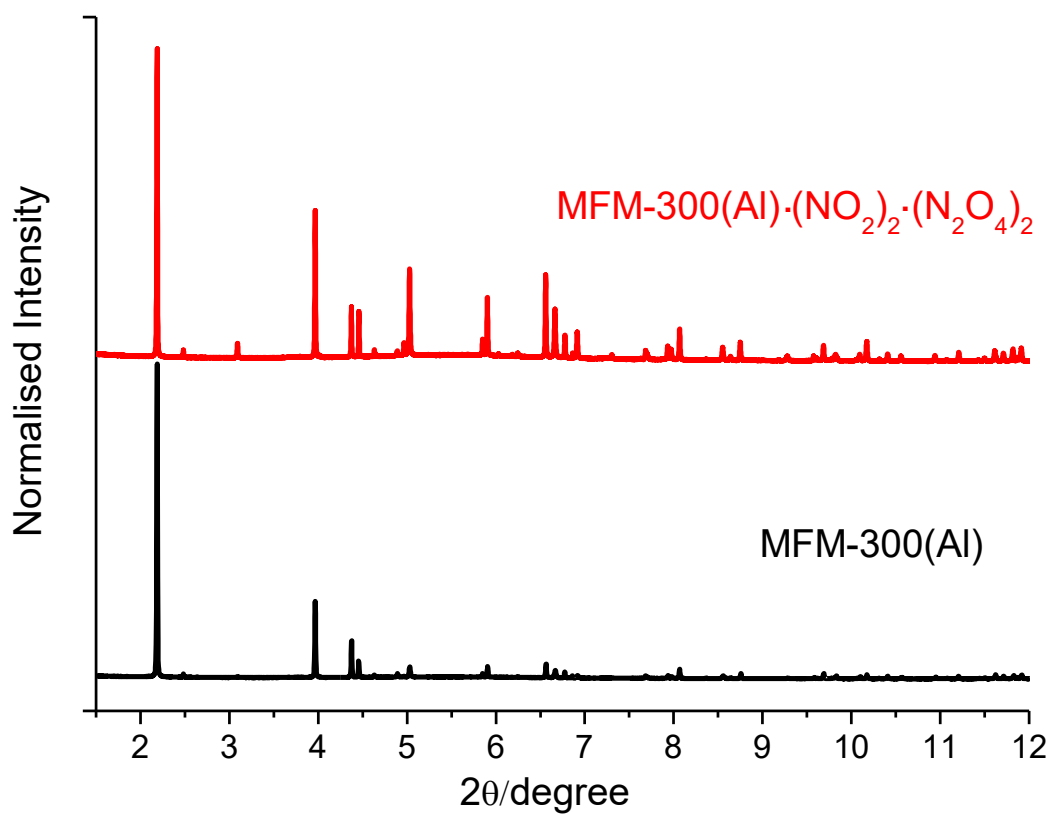
a
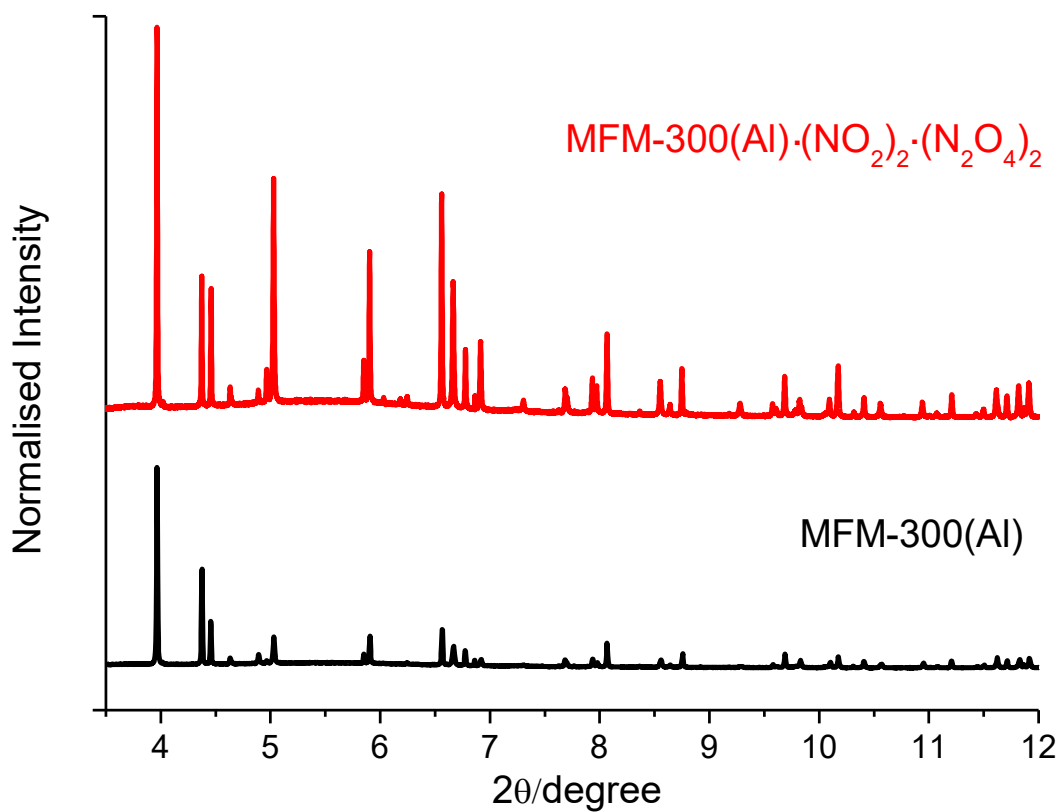
b

Figure S3. (a) Comparison of powder X-ray diffraction patterns for desolvated and NO_2-loaded MFM-300(Al) samples at 298 K [$\lambda = 0.399999(2)$ Å]; (b) higher angle data ($2\theta = 3.5\text{-}12^\circ$) has been scaled up confirming that MFM-300(Al) retains high crystallinity on uptake of NO_2, which also induces significant changes on the intensities of a number of Bragg peaks.
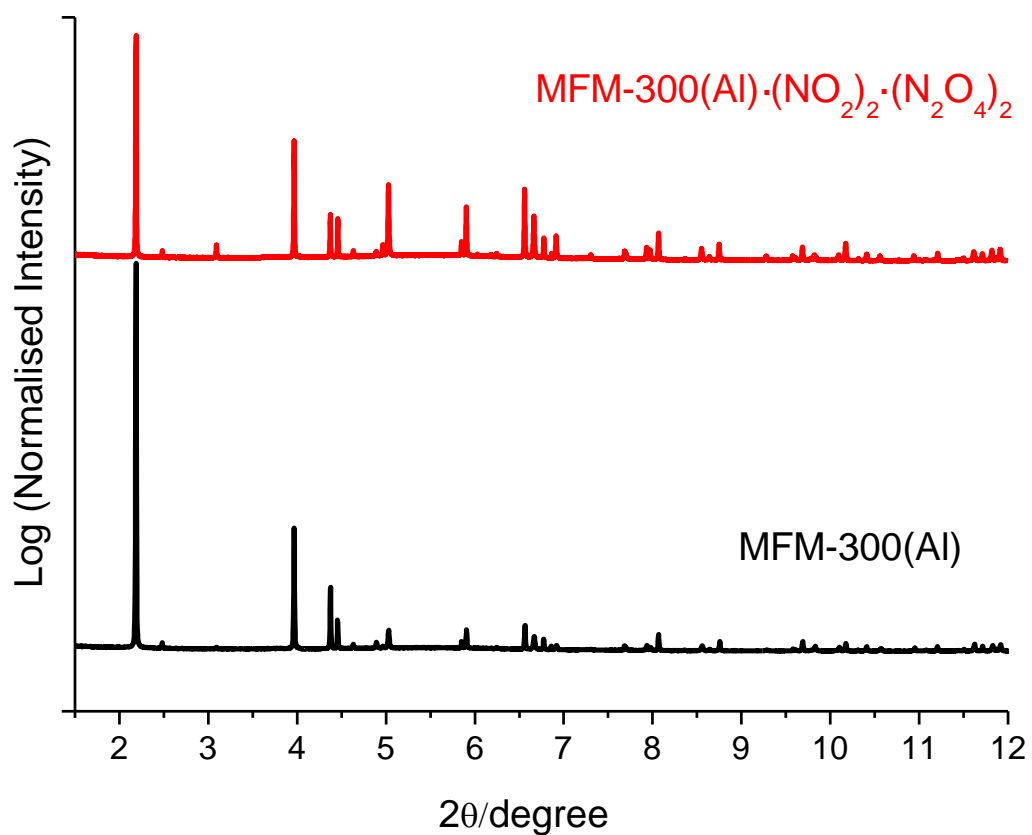
a
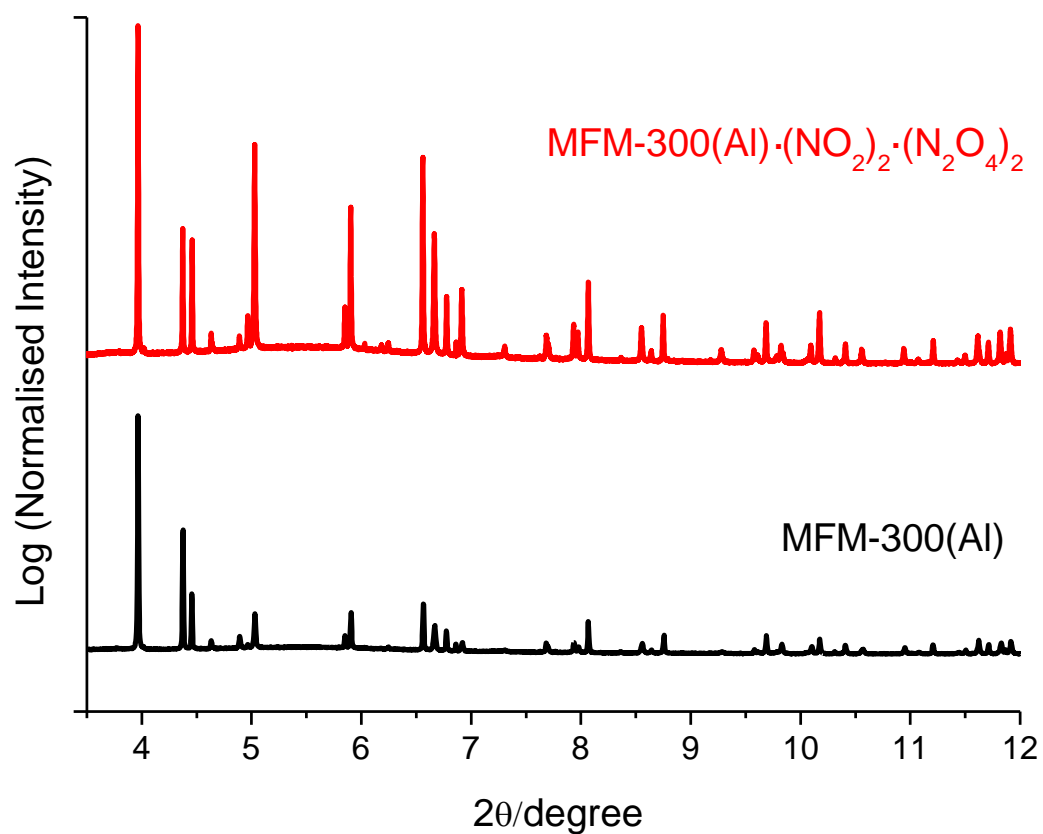
b

Figure S4. Log scale views for (a) comparison of powder X-ray diffraction patterns for desolvated and NO_2-loaded MFM-300(Al) samples at 298 K [λ = 0.399999(2) Å]; (b) higher angle data (2θ = 3.5-12°) has been scaled up confirming that MFM-300(Al) retains high crystallinity on uptake of NO_2, which also induces significant changes on the intensities of a number of Bragg peaks.

a

b

c
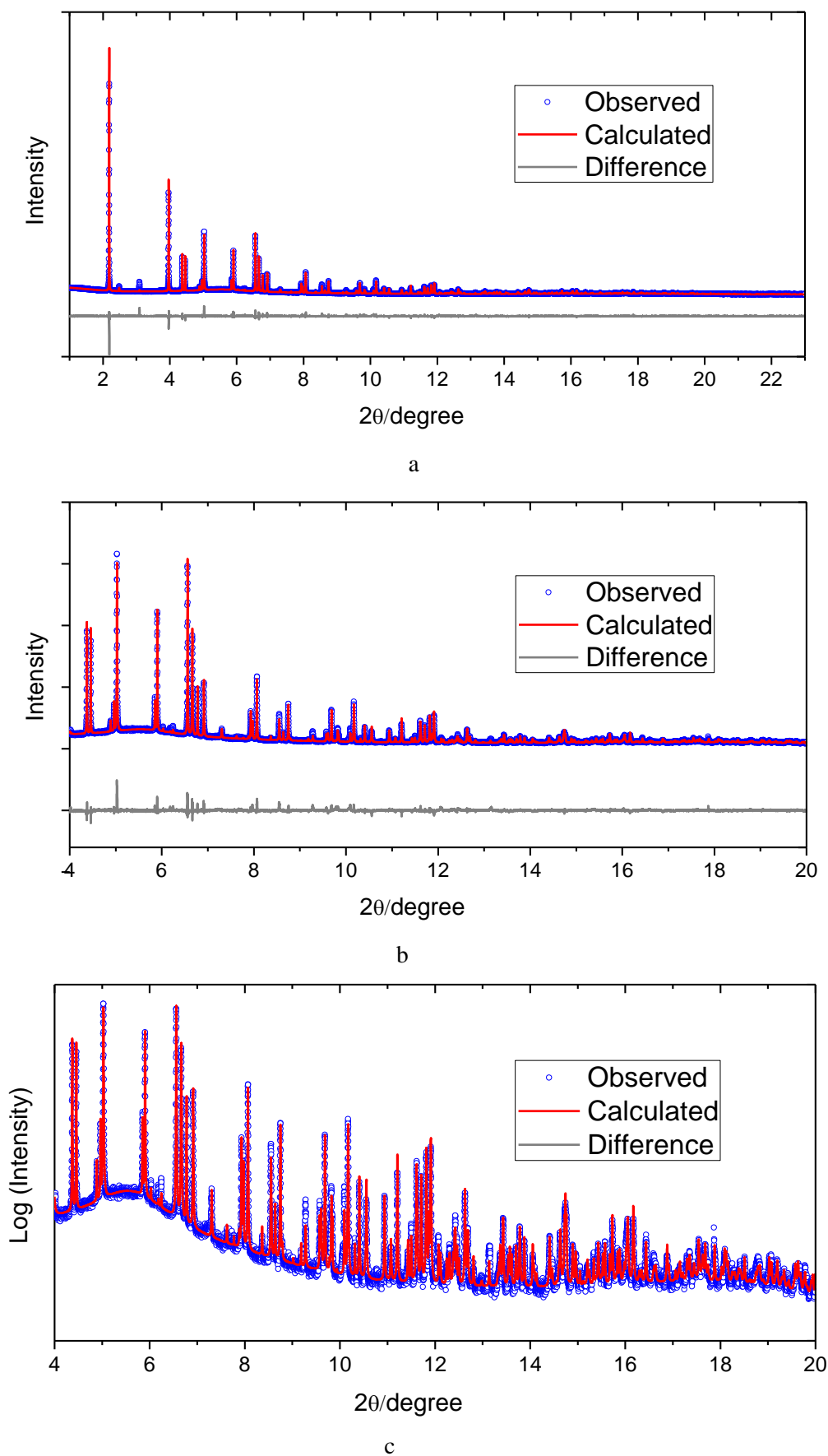
Figure S5. (a) PXRD patterns [observed (blue), calculated (red) and difference (grey)] for the Rietveld refinement of the NO$_2$-loaded MFM-300(Al)·(NO$_2$)$_2$·(N$_2$O$_4$)$_2$ [λ = 0.399999(2) Å]; (b) higher angle data (2θ = 4-20°) scaled up to show the quality of fit between the observed and the calculated patterns; (c) detailed view of the fitting of PXRD patterns in log scale.
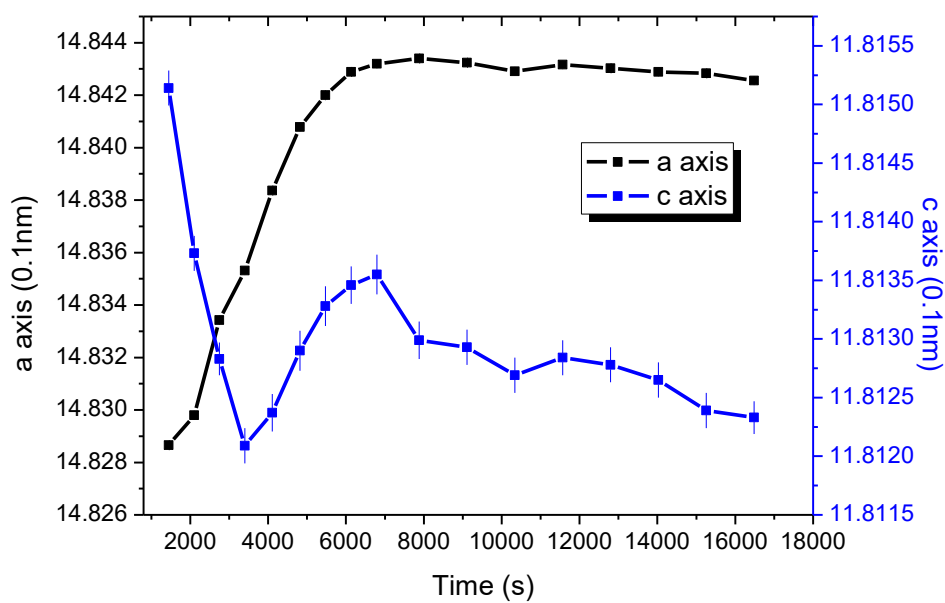
Figure S6. Variation of the lattice parameters (*a* and *c* axis) of MFM-300(Al) upon NO_2 loading at 1 bar and 298 K (where the error bar is invisible, the error bar is smaller than the data symbol).
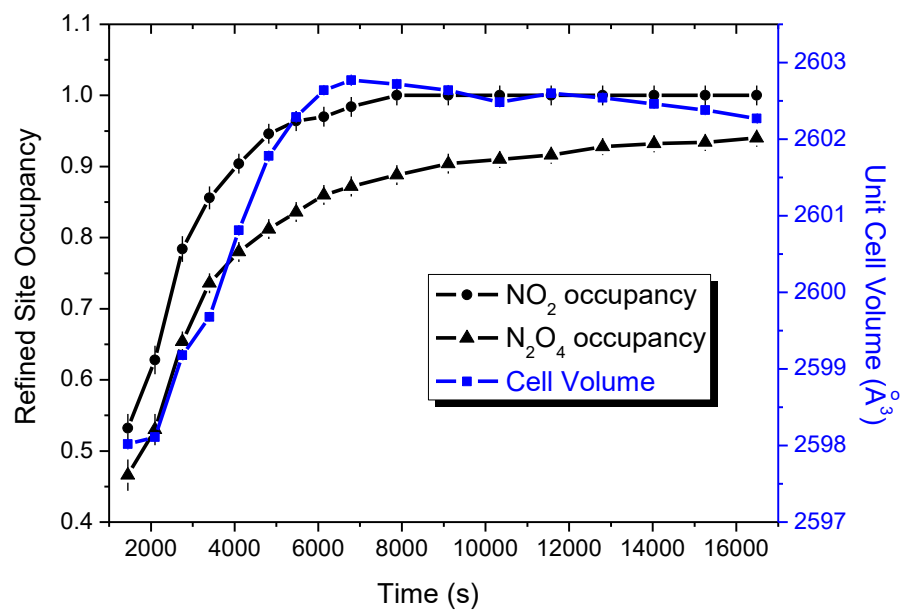
Figure S7. Variation of the lattice parameters (cell volume) and site occupancies of NO_2 and N_2O_4 within MFM-300(Al) as a function of time (where the error bar is invisible, the error bar is smaller than the data symbol).

Table S3. Variations of the cell parameters and site occupancies for MFM-300(Al)·$(NO_2)_2$·$(N_2O_4)_2$ as a function of time upon NO_2 loading at 298 K and 1 bar.

Time (s)	a (Å)	c (Å)	cell volume ($Å^3$)	NO_2 occupancy	N_2O_4 occupancy	N_2O_4/NO_2 ratio
1446	14.82866(17)	11.81514(15)	2598.02(7)	0.532(20)	0.466(22)	0.875(52)
2098	14.8298(16)	11.81373(15)	2598.11(7)	0.628(20)	0.530(22)	0.844(44)
2750	14.83343(14)	11.81283(14)	2599.18(6)	0.784(18)	0.654(14)	0.834(26)
3402	14.83531(16)	11.81209(15)	2599.68(6)	0.856(16)	0.736(14)	0.860(23)
4103	14.83836(17)	11.81237(16)	2600.81(7)	0.904(14)	0.780(14)	0.863(20)
4816	14.84079(18)	11.81290(17)	2601.78(7)	0.946(14)	0.812(14)	0.858(19)
5470	14.84200(19)	11.81328(17)	2602.29(8)	0.964(14)	0.836(14)	0.867(19)
6135	14.84289(17)	11.81346(16)	2602.64(7)	0.970(14)	0.860(14)	0.887(19)
6791	14.84320(18)	11.81355(17)	2602.77(7)	0.984(14)	0.872(14)	0.886(19)
7880	14.84340(17)	11.81299(16)	2602.72(7)	1.000(14)	0.888(14)	0.888(19)
9110	14.84324(17)	11.81293(15)	2602.64(7)	1.000(14)	0.904(14)	0.904(19)
10339	14.84291(16)	11.81269(15)	2602.48(6)	1.000(14)	0.910(12)	0.910(19)
11568	14.84317(16)	11.81284(15)	2602.60(6)	1.000(14)	0.916(12)	0.916(19)
12798	14.84303(17)	11.81278(15)	2602.54(7)	1.000(14)	0.928(12)	0.928(19)
14028	14.84289(16)	11.81265(15)	2602.46(7)	1.000(14)	0.932(12)	0.932(19)
15257	14.84283(17)	11.81239(15)	2602.38(7)	1.000(14)	0.934(12)	0.934(19)
16487	14.84256(14)	11.81233(14)	2602.27(6)	1.000(14)	0.940(12)	0.940(19)

3. Additional Views of Crystal Structures

a   b
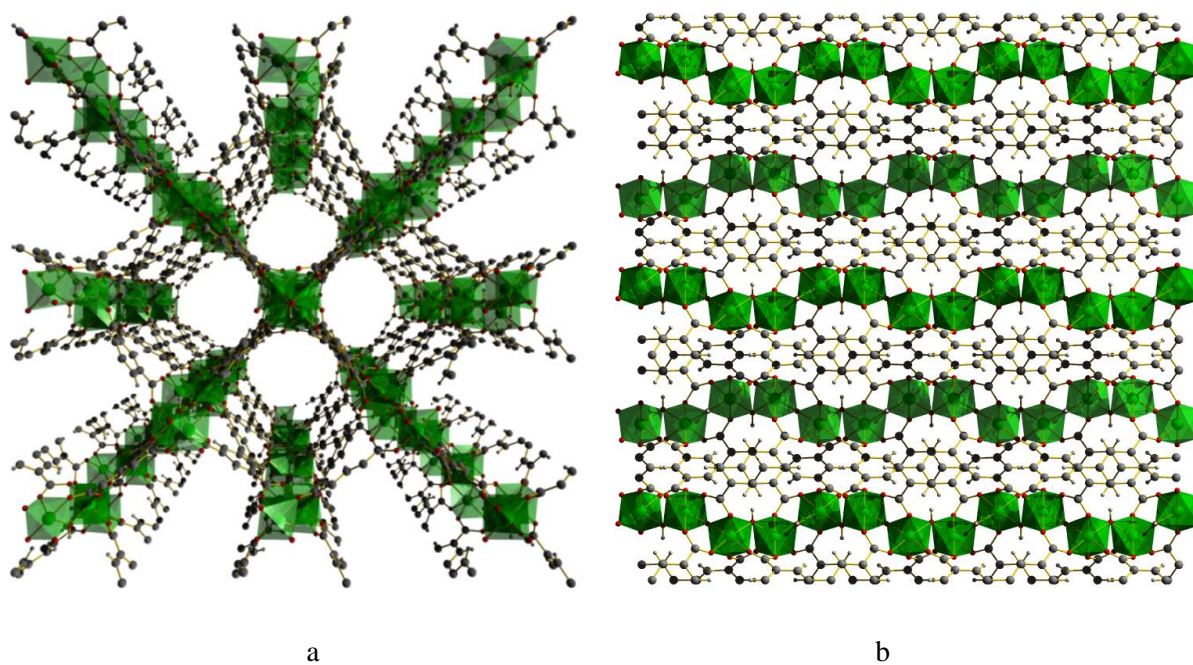
Figure S8. View of the structure for desolvated MFM-300(Al) (a) along the c-axis and (b) along the a-axis. The μ_2-(OH) groups protrude into the centre of the channel from four directions. (Al: green; carbon: grey; oxygen: red; hydrogen: white; [AlO$_4$(OH)$_2$]: green octahedron).

a	b
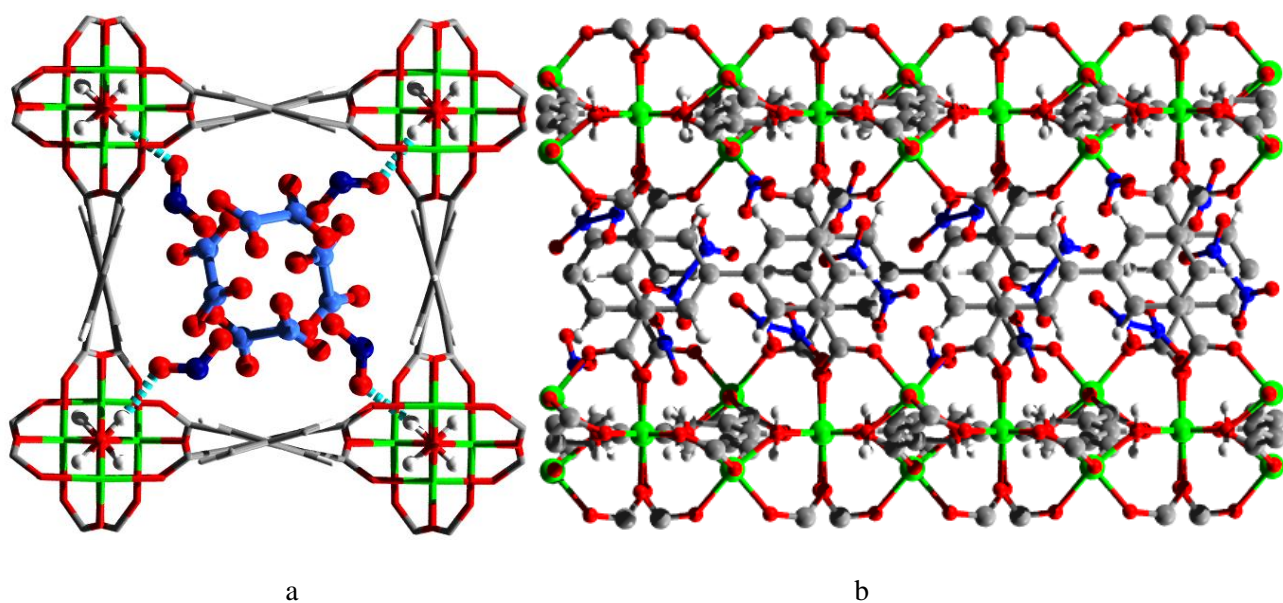
Figure S9. View of the structure of MFM-300(Al)·$(NO_2)_2$·$(N_2O_4)_2$ (a) along the *c*-axis and (b) along the *a*-axis (Al: green; carbon: grey; oxygen: red; hydrogen: white; nitrogen: blue). The structure was obtained by DFT calculation. NO_2 and N_2O_4 molecules in the channel and the host functional groups involved in cooperative binding are highlighted by the use of ball-and-stick mode. The N atoms of NO_2 and N_2O_4 are highlighted in deep and light blue, respectively.
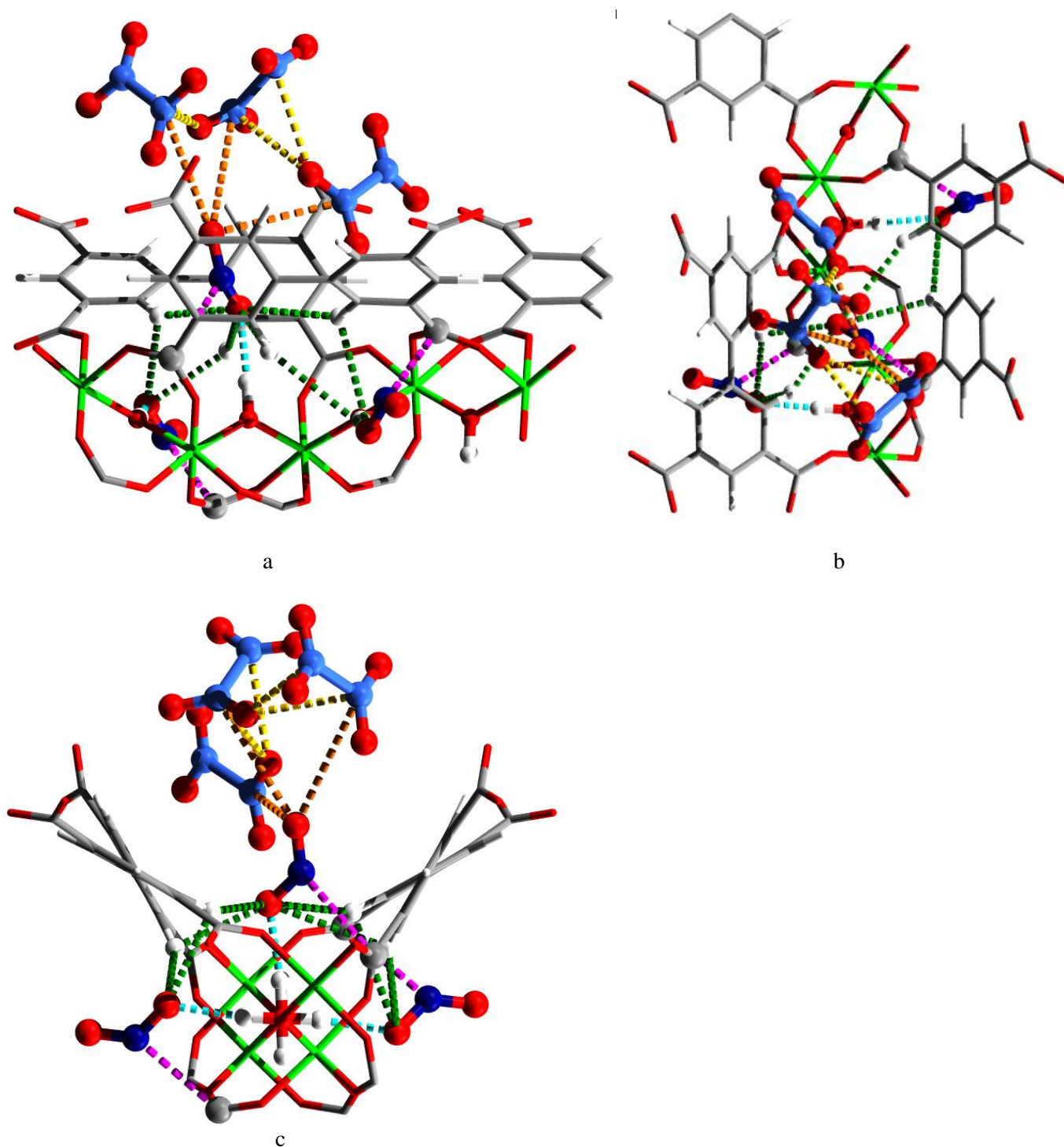
Figure S10. Detailed views of -OH, -CH, and carboxylate groups binding NO_2 and N_2O_4 molecules in the functionalised cavity of MFM-300(Al)·$(NO_2)_2$·$(N_2O_4)_2$. Views along (a) the *a*-axis, (b) the *b*-axis and (c) the *c*-axis (Al: green; carbon: grey; oxygen: red; hydrogen: white; nitrogen: blue). The structure was obtained by DFT calculation. NO_2 and N_2O_4 molecules in the channel and the host functional groups involved in cooperative binding are highlighted by the use of ball-and-stick mode. The O···HO hydrogen-bonds, C···N dipole, H···O supramolecular interactions, and inter-molecular dipole interactions (O^m···N^d and N^d···O^d, where m and d represents for monomer and dimer, respectively) are highlighted in cyan, purple, green, orange and yellow, respectively. The N atoms of NO_2 and N_2O_4 are highlighted in deep and light blue, respectively.

a

b

c

Figure S11. Detailed views of -OH, -CH, and carboxylate groups binding monomer NO_2 molecules in the functionalised cavity of MFM-300(Al)·$(NO_2)_2$·$(N_2O_4)_2$. Views along (a) the *a*-axis, (b) the *b*-axis and (c) the *c*-axis (Al: green; carbon: grey; oxygen: red; hydrogen: white; nitrogen: blue). The structure was obtained by DFT calculation. NO_2 molecules in the channel and the host functional groups involved in cooperative binding are highlighted by the use of ball-and-stick mode. The O···HO hydrogen-bonds, C···N dipole and H···O supramolecular interactions are highlighted in cyan, purple and green, respectively.

a

b
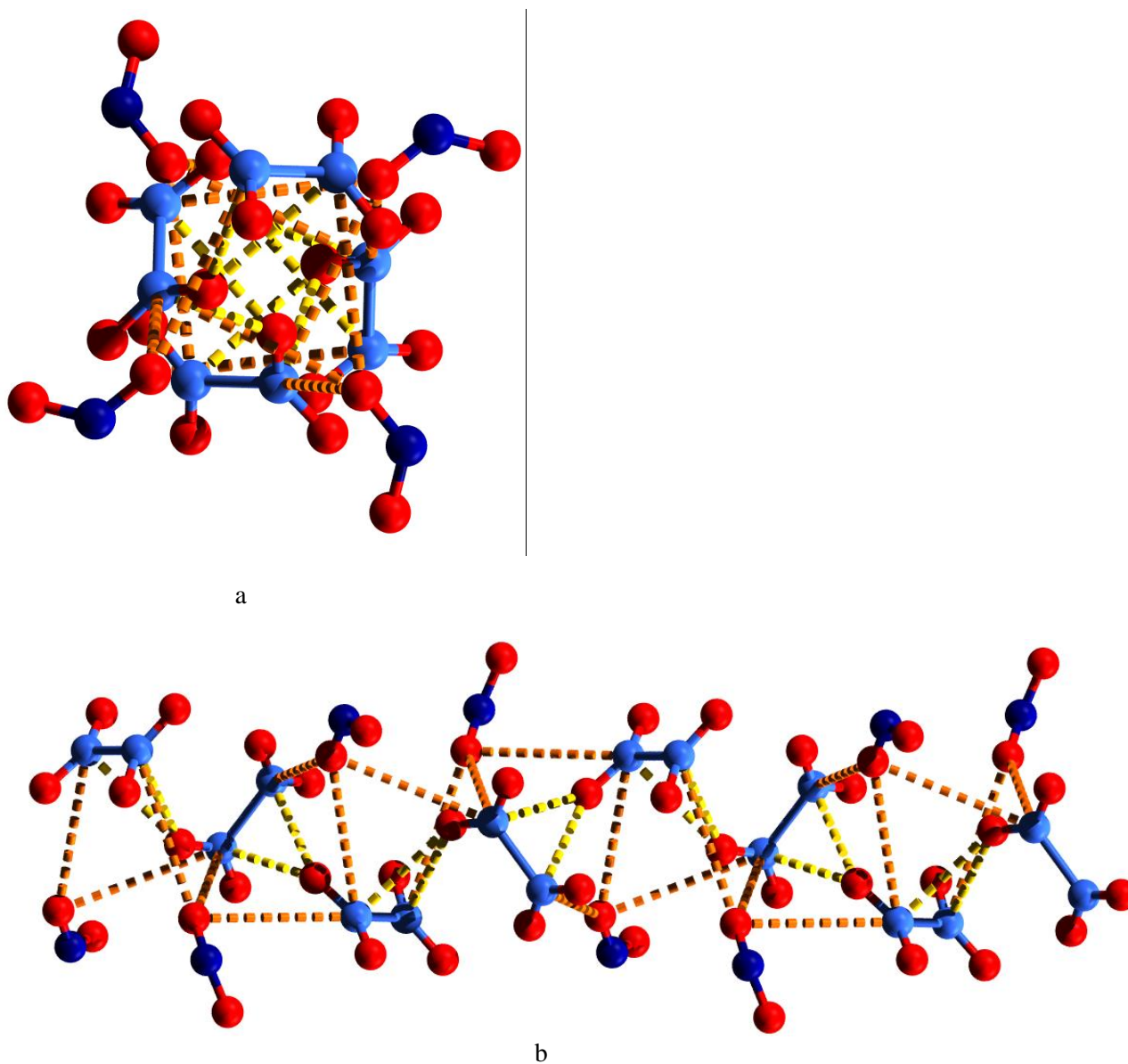
Figure S12. Detailed views of the intermolecular helical chain of NO_2 and N_2O_4 molecules within the functionalised cavity of MFM-300(Al)·$(NO_2)_2$·$(N_2O_4)_2$. Views along (a) the *c*-axis and (b) the *a*-axis (oxygen: red; nitrogen: blue). The structure was obtained by DFT calculation. The inter-molecular dipole interactions ($O^m \cdots N^d$ and $N^d \cdots O^d$, where m and d represents for monomer and dimer, respectively) are highlighted in orange and yellow, respectively. The N atoms of NO_2 and N_2O_4 are highlighted in deep and light blue, respectively.

a	b
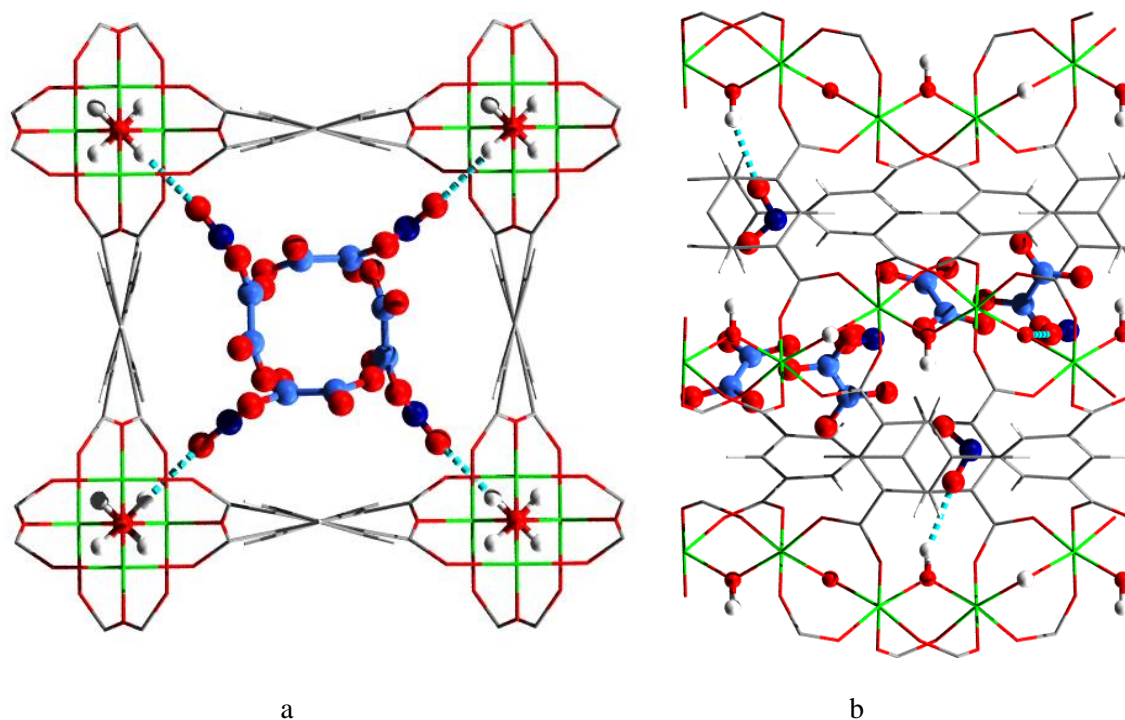
Figure S13. View of the structure of MFM-300(Al)·(NO$_2$)$_2$·(N$_2$O$_4$)$_2$ (a) along the *c*-axis and (b) along the *a*-axis (Al: green; carbon: grey; oxygen: red; hydrogen: white; nitrogen: blue). The structure was obtained by synchrotron PXRD refinement. NO$_2$ and N$_2$O$_4$ molecules in the channel and the host functional groups involved in cooperative binding are highlighted by the use of ball-and-stick mode. The N atoms of NO$_2$ and N$_2$O$_4$ are highlighted in deep and light blue, respectively.

a

b

c
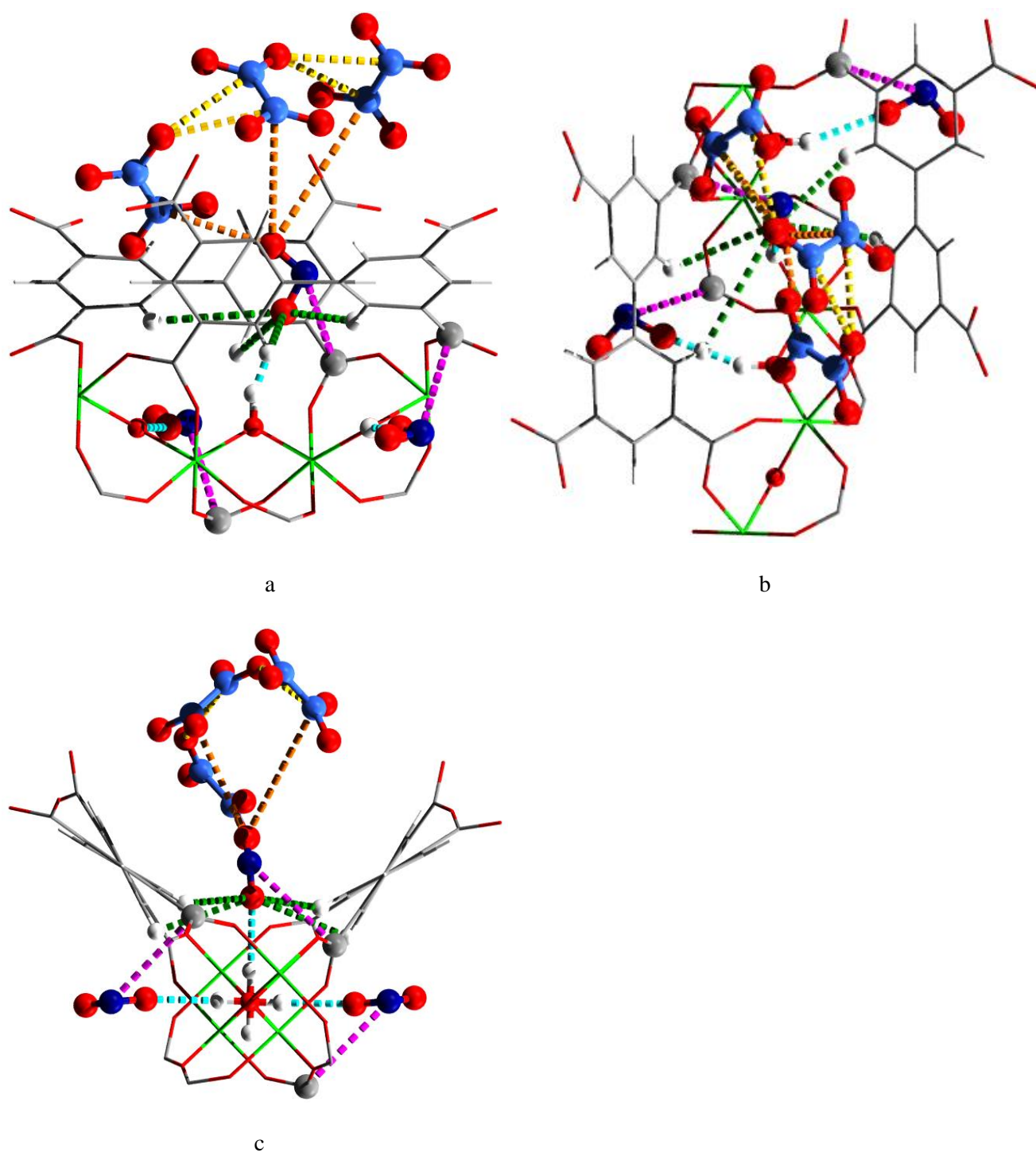
Figure S14. Detailed views of -OH, -CH, and carboxylate groups binding NO_2 and N_2O_4 molecules in the functionalised cavity of MFM-300(Al)·$(NO_2)_2$·$(N_2O_4)_2$. Views along (a) the *a*-axis, (b) the *b*-axis and (c) the *c*-axis (Al: green; carbon: grey; oxygen: red; hydrogen: white; nitrogen: blue). The structure was obtained by synchrotron PXRD refinement. NO_2 and N_2O_4 molecules in the channel and the host functional groups involved in cooperative binding are highlighted by the use of ball-and-stick mode. The O···HO hydrogen-bonds, C···N dipole, H···O supramolecular interactions, and inter-molecular dipole interactions (O^m···N^d and N^d···O^d, where m and d represents for monomer and dimer, respectively) are highlighted in cyan, purple, green, orange and yellow, respectively. The nitrogen atoms of NO_2 and N_2O_4 are highlighted in deep and light blue, respectively.

a

b

c

Figure S15. Detailed views of -OH, -CH, and carboxylate groups binding monomer NO_2 molecules in the functionalised cavity of MFM-300(Al)·$(NO_2)_2$·$(N_2O_4)_2$. Views along (a) the *a*-axis, (b) the *b*-axis and (c) the *c*-axis (Al: green; carbon: grey; oxygen: red; hydrogen: white; nitrogen: blue). The structure was obtained by synchrotron PXRD refinement. NO_2 molecules in the channel and the host functional groups involved in cooperative binding are highlighted by the use of ball-and-stick mode. The O···HO hydrogen-bonds, C···N dipole and H···O supramolecular interactions are highlighted in cyan, purple and green, respectively.

a

b
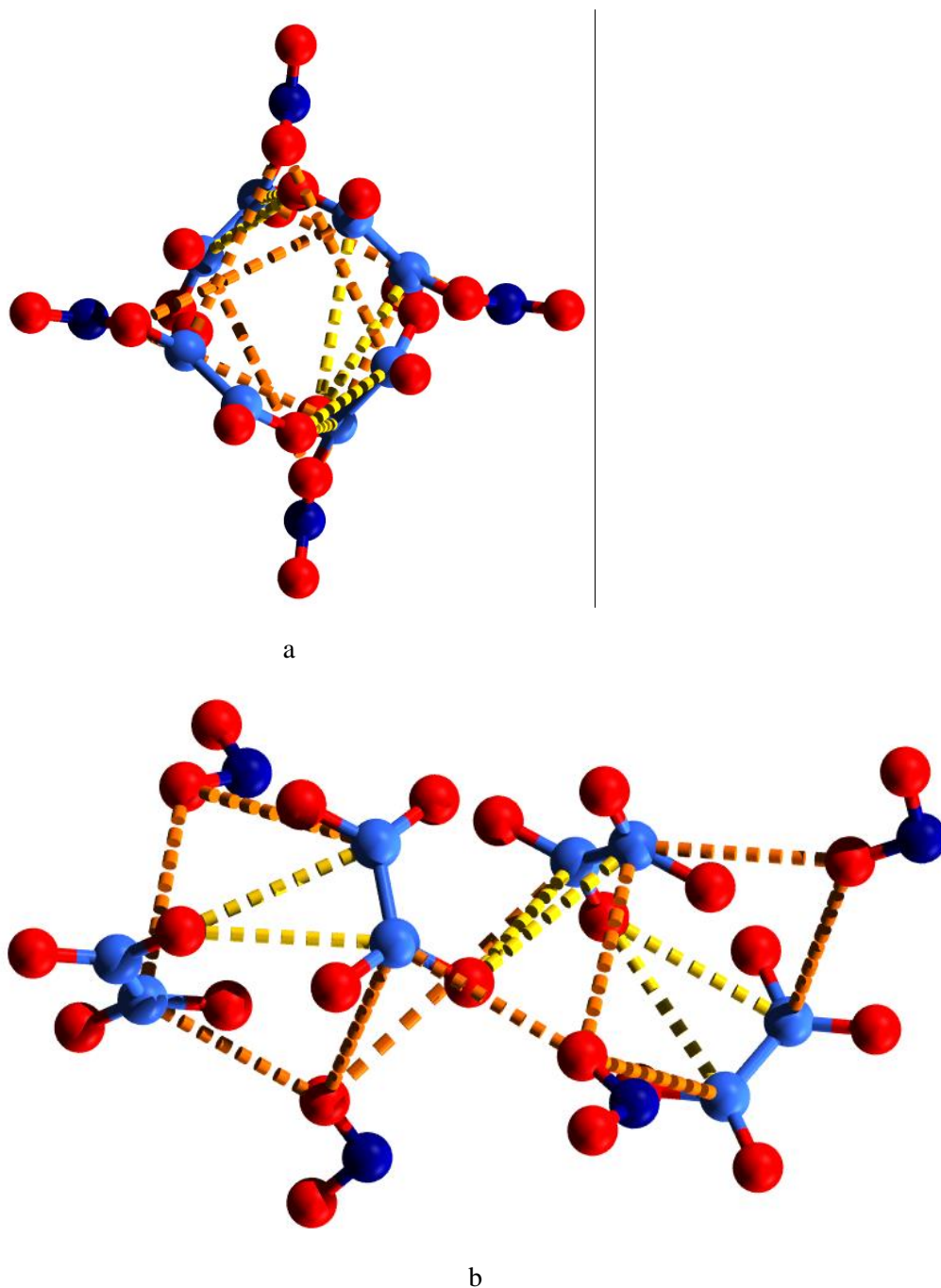
Figure S16. Detailed views of the intermolecular helical chain of NO_2 and N_2O_4 molecules within the functionalised cavity of MFM-300(Al)·$(NO_2)_2$·$(N_2O_4)_2$. Views along (a) the *c*-axis and (b) the *a*-axis (oxygen: red; nitrogen: blue). The structure was obtained by synchrotron PXRD refinement. The inter-molecular dipole interactions (O^m···N^d and N^d···O^d, where m and d represents for monomer and dimer, respectively) are highlighted in orange and yellow, respectively. The nitrogen atoms of NO_2 and N_2O_4 are highlighted in deep and light blue, respectively.

a   b
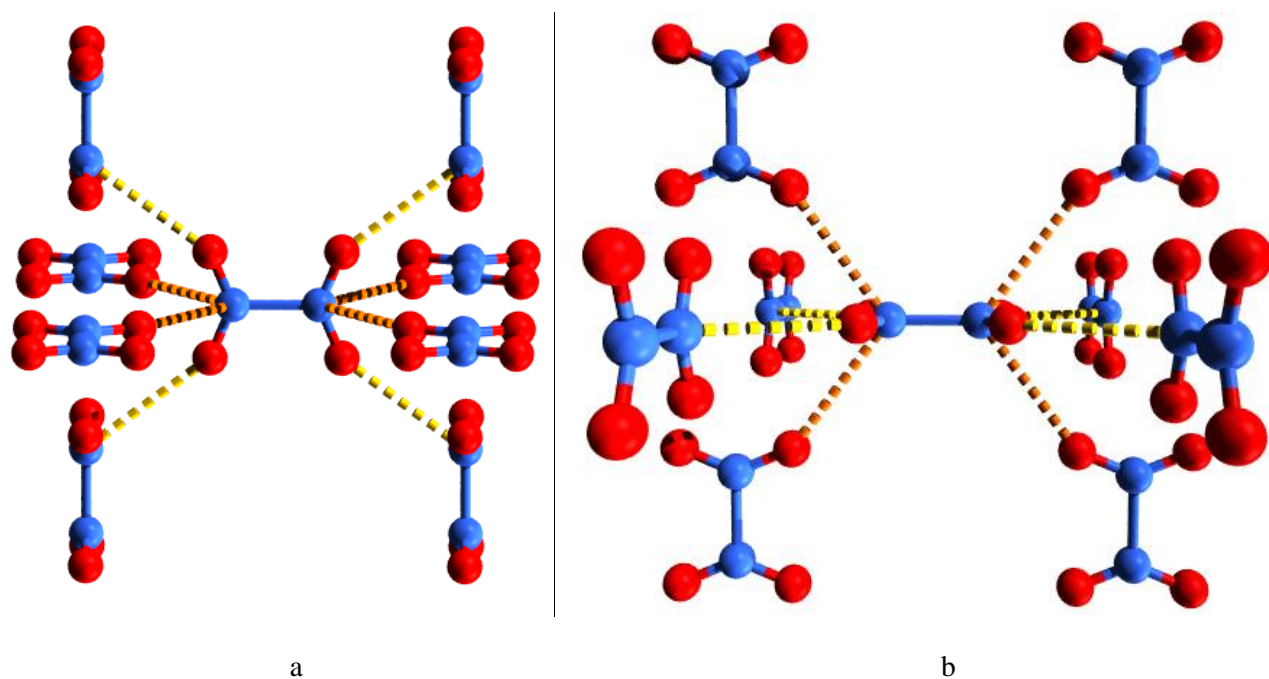
Figure S17. Detailed views of the crystal structure of N_2O_4 determined by neutron diffraction at 20 K. Views along (a) the *c*-axis and (b) the *b*-axis (oxygen: red; nitrogen: blue). Each N_2O_4 molecule is surrounded by eight neighbouring N_2O_4 molecules *via* intermolecular dipole interactions (O$\cdots$N = 3.13Å and N$\cdots$O = 3.13 Å, which are highlighted in yellow and orange, respectively). The density of solid N_2O_4, calculated based upon the crystal structure at 20 K, is 2.01 g cm^{-3}.

4.   Additional Gas Sorption Isotherm Plots for MFM-300(Al)
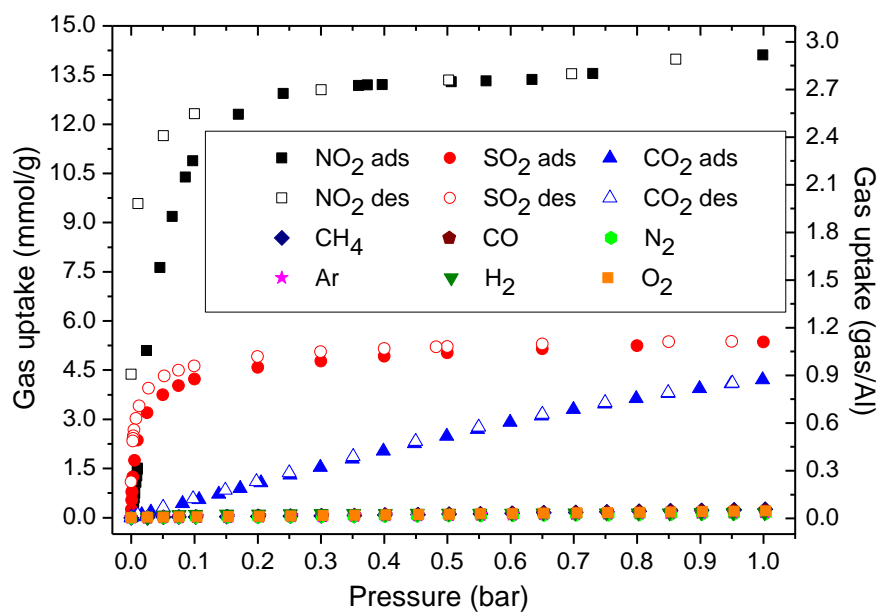
Figure S18. Adsorption isotherms for NO_2, SO_2, CO_2, N_2, CH_4, Ar, CO, O_2 and H_2 in MFM-300(Al) at 298 K up to 1.0 bar. The lack of CO adsorption in MFM-300(Al) at 298 K and 1.0 bar when comparing to CO_2 is likely due to its larger kinetic diameter (3.76 Å and 3.30 Å for CO and CO_2, respectively) and weaker interaction (quadruple moment of -8.58 x 10^{-40} C m^2 and -13.4 x10^{-40} C m^2 for CO and CO_2, respectively) to the MOF host.
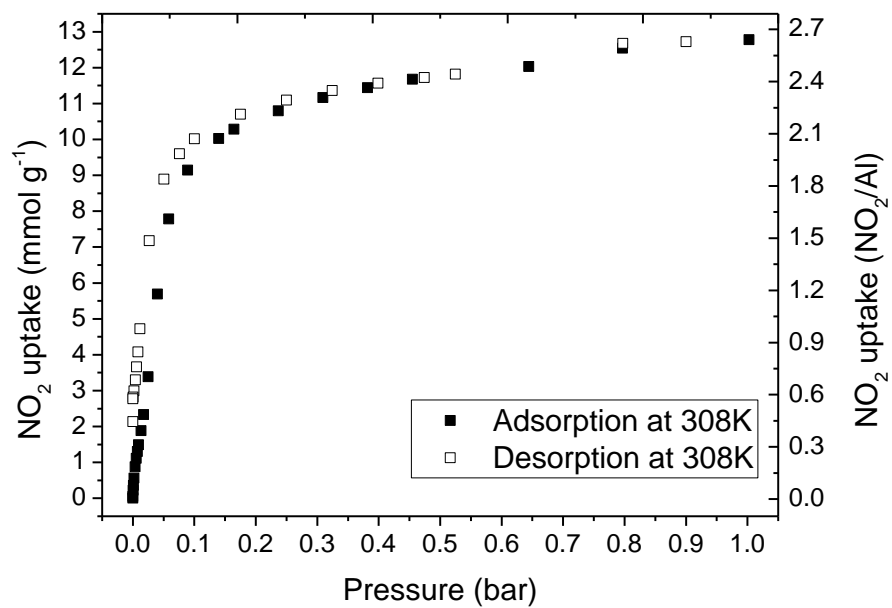
Figure S19. Adsorption isotherms for NO_2 in MFM-300(Al) at 308 K up to 1.0 bar.
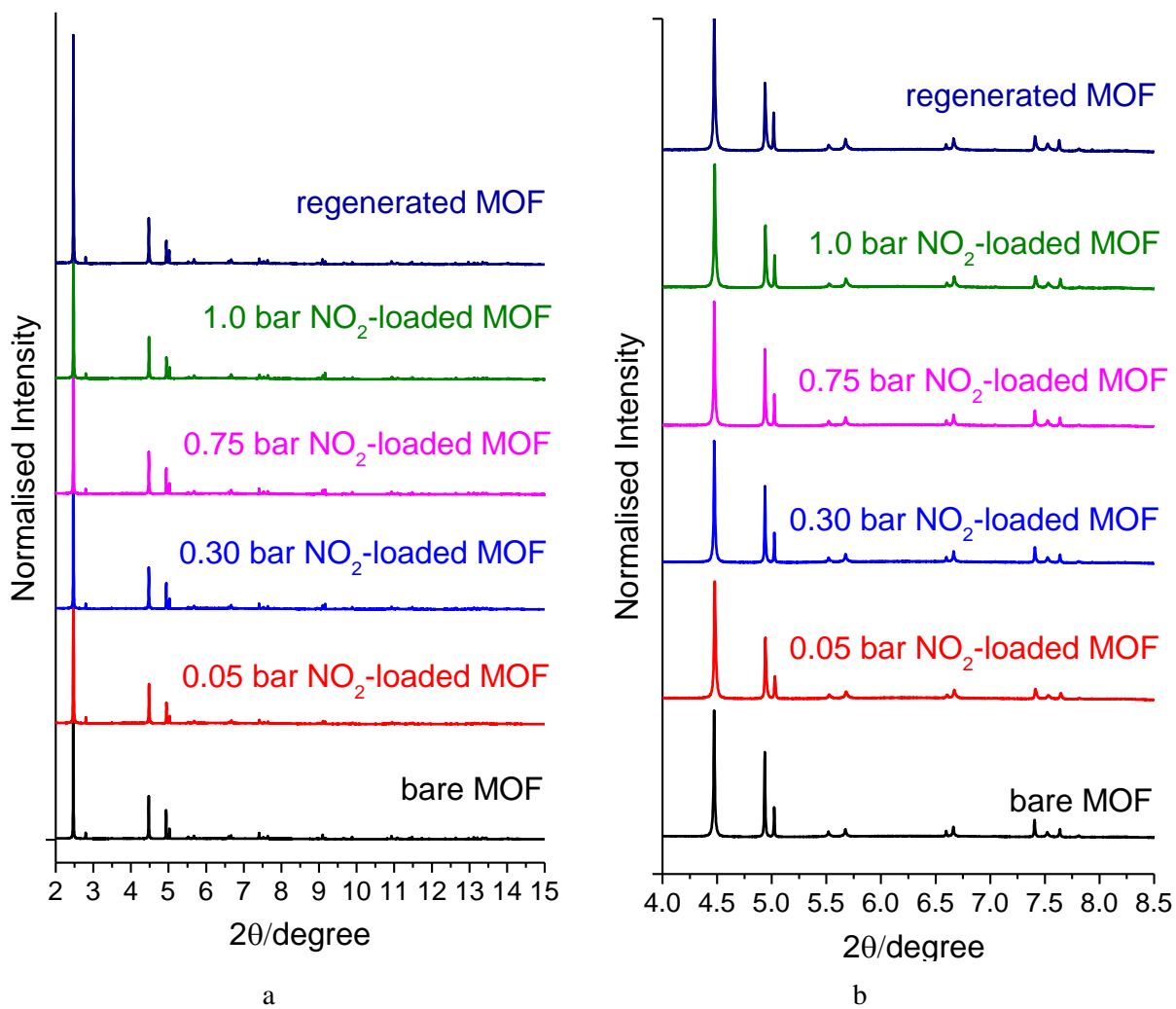
Figure S20. (a) Comparison of powder synchrotron X-ray diffraction patterns for desolvated and NO_2-loaded MFM-300(Al) samples at 308 K under varying NO_2 pressure [λ = 0.45087056(2) Å]; (b) higher angle data (2θ = 4-8.5°) has been scaled up, confirming the absence of structural transitions of MFM-300(Al) on uptake of NO_2 at 308 K.
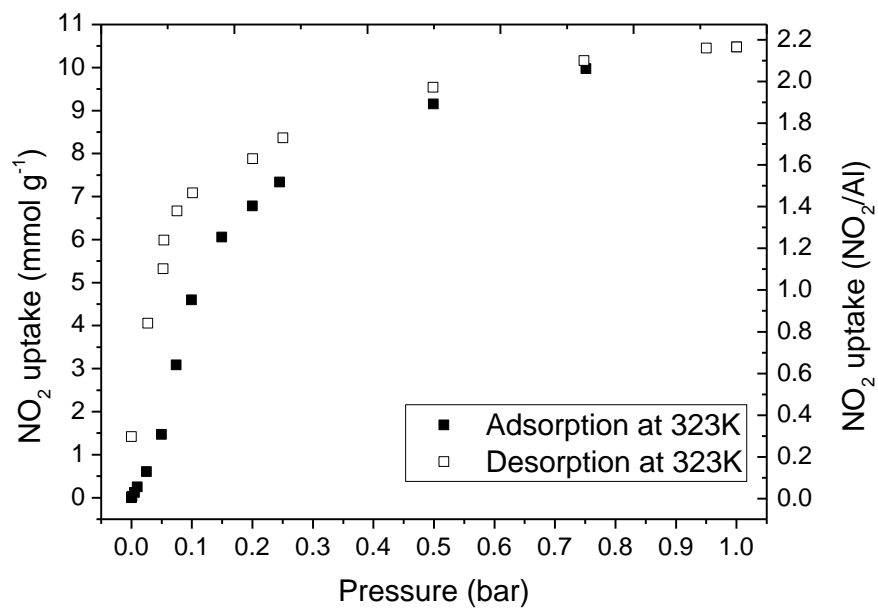
Figure S21. Adsorption isotherms for NO_2 in MFM-300(Al) at 315.5 K up to 1.0 bar. [to be updated]
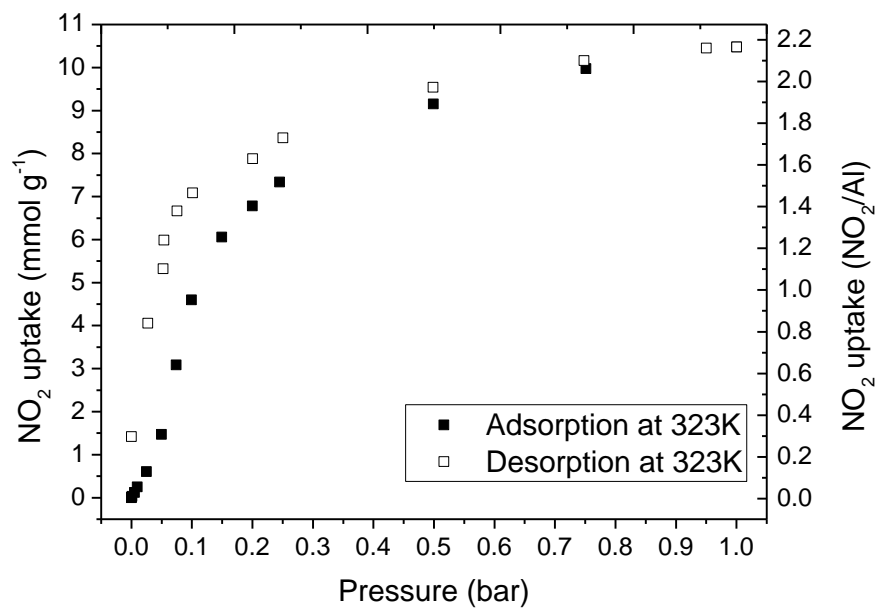
Figure S22. Adsorption isotherms for NO_2 in MFM-300(Al) at 323 K up to 1.0 bar.
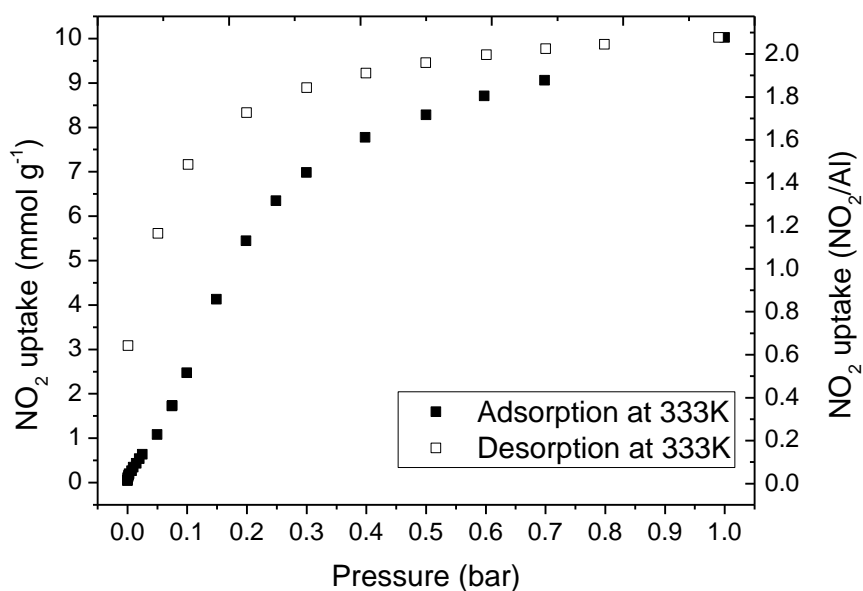
Figure S23. Adsorption isotherms for NO_2 in MFM-300(Al) at 333 K up to 1.0 bar.

The hysteresis of NO_2 adsorption-desorption in MFM-300(Al) increases slightly with increased temperature (298-333 K). This is likely due to the presence of stronger host-guest interaction at higher temperatures owing to the highly reactive nature of NO_2. Interestingly, similar observation has been recently reported for CO adsorption in a nickel-based MOF which showed broader hysteresis at high temperature due to the presence of strong MOF-CO interaction at high temperature[9].

5. **Analysis of breakthrough data of diluted NO$_2$ gas streams in porous materials reported in the literature**

The breakthrough of diluted NO$_2$ gas streams (500-2138 ppm in air or N$_2$ as a carrier gas) has been tested for a number of MOFs, metal-doped MOFs, MOF/graphite oxides and the BPL carbon materials[10-16]. Some of these tests have been conducted *via* microbreakthrough experiments in which typically 10-20 mg sample was used to assemble a fixed-bed of sorbent. Some of the tests have been carried out in both dry and wet conditions, with the carrier gas mixture containing water vapour. The maximum uptake capacity of NO$_2$ in a given system was obtained by the integration of the breakthrough plots, and the experimental details and results of the reported breakthrough data are summarized in Table S4. The BET surface and pore volume for each material have been included in Table S4, and where these data are not reported in the original paper, data for the same material reported elsewhere have been used for the analysis.

The density for liquid NO$_2$, liquid N$_2$O$_4$ and solid N$_2$O$_4$ is 1.45 g cm^{-3} at 294 K, 1.44 g cm^{-3} at 294 K, and 1.94 g cm^{-3} at 140 K, respectively. The density of solid NO$_2$ is not available in the literature, presumably since condensation (usually *via* cooling) lead to dimerisation of monomers to N$_2$O$_4$ in the solid state. Gurvitsch's rule states that the amount of substrate adsorbed at relative pressures close to 1.0 corresponds to complete filling of the available pore volume and when expressed as a liquid volume is very similar for all adsorbates. The maximium equilibrium adsorption capacity for physisorption of gases/vapors on a given porous material can be estimated by the product of pore volume and the liquid density of the adsorbate based upon a pore filling model. This assumes the following: (i) there is no distortion of the host structure upon guest inclusion; (ii) all pore space is accessible to the guest molecules; (iii) there is no formation of a chemical bond between the host and guest. Thus, the theoretical maximium equilibrium adsorption capacities of NO$_2$ gas in all reported materials have been calculated using liquid density of NO$_2$ at 294 K. For comparison, similar calculations have also been performed using the solid N$_2$O$_4$ density at 140 K. In theory, the maximium gas adsorption uptake of a given material is the upper limit of the corresponding fixed-bed packed of the pure material and can be compared with the experimental uptakes.

In general, the expermental uptakes are much lower than the uptakes calculated using the pore volume and adsorbate densities (entries 5-17, Table S4). This could be due to a number of factors: (i) a host-guest adsorption equilibrium has not been fully established under the dynamic breakthrough measurements due to kinetic limitations; (ii) host samples suffer from structural stability issues, which reduce the accessible pore space; (iii) the theoretical uptakes were calculated based on pure gas/vapor adsorption, whereas the breakthrough experiments were conducted with ppm level of NO$_2$ gas (subject to uncertainties on concentration) and high pressure may be required to achieve the saturation; and (iv) the existence of competition between NO$_2$ and components in the carrier gas (*e.g.*, minor O$_2$, N$_2$, CO$_2$, H$_2$O); (v) fixed-bed used in breakthrough experiment was assembled under compression and thus the diffusion through the sample grains can be notably different to the powder sample used in isotherm experiments.

These factors together lead to the typical observation that expermental results are lower than those calculated using the pore volume and adsorbate densities (entries 5-17, Table S4), and the estimated uptake from breakthrough measurement using ppm level eluent can carry large uncertainties. However, entries 2 and 3 (Table S4) have the experimental maximium gas uptakes exceeding the maximum calculated from the pore volume. Such results cannot be explained by conventional adsorption theory with capillary condensation in the pores. In addition, under wet conditions, the NO_2 uptakes are higher than those calculated using solid N_2O_4 density at 140 K. Interestingly, in entries 1-4 (Table S4), there is a notable enhancement (up to 4 times) on the NO_2 adsorption capacity under wet conditions in comparison to dry conditions. It has been proposed that under wet conditions, a water film can be formed on top of the MOF samples and NO_2 then dissolves in the water film to give nitrous/nitric acid leading to unpredictable uptake capacities[13]. Also, it is possible that H_2O and NO_2 interact within the pores. Thus, accurate measurement of NO_2 adsorption in the presence of moisture is a highly challenging task, not least because the strong interaction between NO_2 and water (mostly solvation to form acids) taking place inside the MOF pores, on the MOF surface and within the adsorption system (such as pipes and dead volume of reactors). The latter two can hardly be quantified from experiment, likely leading to unpredictable results.

It is difficult to compare capacities of various materials because of the use of different experimental conditions (temperature, NO_2 concentrations, adsorbent amounts, reactor size). There is also the problem where porous materials have the same designation but may have been activated under different conditions. Some reports do not provide basic gas adsorption characterization data for the porous structure of the samples studied. Table S4 shows NO_2 breakthrough for UiO-66 where both samples have similar BET surface areas and total pore volumes (entries 7 and 9); however, the NO_2 capacities under dry conditions differ by a factor of ~2.4. We also noted marked inconsistencies between other reports for testing nominally the same host adsorbent material. Table S4 includes NO_2 breakthrough data entries 1 (micro-breakthrough experiments with no pore structure characterisation data available), 7 (breakthrough) and 9 (micro-breakthrough) for UiO-66 and entries 3 (micro-breakthrough) and 5 (breakthrough) for HKUST-1. For UiO-66 under dry conditions the breakthrough capacity has been recorded as 8.8, 1.59 and 3.8 mmol g^{-1} in these three studies. The NO_2 uptake capacity under wet condition has been reported as 13.2 and 0.87 mmol g^{-1} from two separate studies (entries 1 and 7). Similarly for HKUST-1, a difference in the NO_2 capacity under wet conditions as large as 22.5 times has been observed [26.4 mmol g^{-1} (microbreakthrough) *versus* 1.17 mmol g^{-1} (breakthrough)]. We therefore conclude that the results from (micro)breakthrough experiments cannot be compared directly with the current isotherm adsorption experiments (entry 18) using pure NO_2.

Table S4. Summary of the breakthrough tests of diluted NO_2 gas in MOFs, metal-doped MOFs, MOF/graphite oxide composites and activated carbon materials in the literature.

	MOF	BET surface area (m^2 g^{-1})	Pore volume (cm^3 g^{-1})	Measurement Method	Sample used to pack fixed-bed	Condition	Experimental capacity (mmol g^{-1})	Theoretical maximum capacity at 294 K[c]	Theoretical maximum capacity at 140 K[d]	Reference
1	UiO-66	990-891[h]	0.426-0.471[h]	microbreakthrough	10-20mg	500-700 ppm NO_2/Air at 293 K	8.8 (dry) 13.2 (wet)	13.4-14.8[a]	18.0-19.9[a]	10
2	UiO-66-NH2	987	0.40	microbreakthrough	10-20mg	500-700 ppm NO_2/Air at 293 K	20.3 (dry) 31.2 (wet)	12.6	16.9	10
3	HKUST-1	909[i]	0.471[i]	microbreakthrough	10-20mg	500-700 ppm NO_2/Air at 293 K	6.5 (dry) 26.1 (wet)	14.8[a]	19.9[a]	10
4	BPL carbon	[b]	[b]	microbreakthrough	10-20mg	500-700 ppm NO_2/Air at 293 K	8.8 (dry) 15.6 (wet)	-	-	10
5	HKUST-1	909	0.471	breakthrough	50-120 mg	1000 ppm NO_2/Air at room temperature	2.30 (dry) 1.17 (wet)	14.8	19.9	11,12
6	HKUST-1/GO	989-1002	0.515-0.566	breakthrough	50-120 mg	1000 ppm NO_2/Air at room temperature	2.43-2.91 (dry) 0.83-1.28 (wet)	16.2-17.8	21.7-23.8	11,12
7	UiO-66	891	0.471	breakthrough	[b]	1000 ppm NO_2/Air at room temperature	1.59 (dry) 0.87 (wet)	14.8	19.9	13
8	UiO-67	1372	0.707	breakthrough	[b]	1000 ppm NO_2/Air at room temperature	1.72 (dry) 2.56 (wet)	22.3	29.8	13
9	UiO-66	990	0.426[g]	microbreakthrough	10-15mg	2138 ppm NO_2	3.8 (dry)	13.4	18.0	14
10	UiO-66-vac	1590	0.666[g]	microbreakthrough	10-15mg	2138 ppm NO_2	3.9 (dry)	21.0	28.1	14
11	UiO-66-ox	1410	0.666[g]	microbreakthrough	10-15mg	2138 ppm NO_2	8.4 (dry)	21.0	28.1	14
12	U-ZrBDC	1070	0.549	breakthrough	[b]	1000 ppm NO_2/Air at room temperature	0.80 (dry) 2.2(wet)	17.3	23.1	15
13	M-ZrBDC	6	0.004	breakthrough	[b]	1000 ppm NO_2/Air at room temperature	0.06 (dry) 0.22(wet)	0.126	0.169	15
14	U-ZrBDPC	2040	0.984	breakthrough	[b]	1000 ppm NO_2/Air at room temperature	1.61 (dry) 3.35(wet)	31.0	41.5	15
15	M-ZrBDPC	75	0.192	breakthrough	[b]	1000 ppm NO_2/Air at room temperature	0.89 (dry) 2.02(wet)	6.05	8.10	15
16	Ce-UiO-66	1035	0.515	breakthrough	[b]	1000 ppm NO_2/Air at room temperature	2.07 (dry) 1.15(wet)	16.2	21.7	16

| 17 | Ce-UiO-67 | 2302 | 1.133 | breakthrough | [b] | 1000 ppm NO_2/Air at room temperature | 1.87 (dry) 1.85 (wet) | 35.7 | 47.8 | 16 |
| 18 | MFM-300Al | 1370 | 0.375[e] 0.43[f] | isotherm | 50-70mg | pure NO_2 at 298K and 1 bar | 14.1 (dry) | 11.8[e] 13.6[f] | 15.8[e] 18.1[f] | this work |

a. these values were not included in the original report and numbers from other studies based upon the same material have been used.

b. these values were not reported in the original reports.

c. liquid density of NO_2/N_2O_4 at 294 K is 1.45 g cm^{-3}.

d. solid density of N_2O_4 at 140 K is 1.94 g cm^{-3}.

e. pore volume was obtained from high pressure CO_2 adsorption data at 273 K and 7 bar. This sample does not adsorb N_2 at 77 K due to the narrow pores leading to activated diffusion effects.

f. pore volume was obtained from the X-ray crystal structure *via* analysis with PLATON.

g entries 9-11 estimated from Figure S2 in SI ref 14.

h. these values were not included in the original report and data for the same material from refs 12 and 13 have been used.

i. these values were not included in the original report and data for the same material from refs 10 and 11 have been used.

6. Analysis and Derivation of the Isosteric Heat of Adsorption for adsorption of NO_2

The differential enthalpies (ΔH_n) and entropies of adsorption (ΔS_n) were calculated as a function of the amount adsorbed (n) from the isotherms measured over a range of temperatures using the Clausius-Clapyeron equation, which is given by the following equation (**1**).

$$\ln(p)_n = \frac{\Delta H_n}{RT} - \frac{\Delta S_n}{R}$$
(**1**)

A graph of *ln(p)* versus $1/T$ at constant amount adsorbed allows the differential enthalpy and entropy of adsorption and also the isosteric enthalpy of adsorption ($Q_{st,n}$) to be determined. These results have been summarized in Table S5 and some selected fitting graphs have been shown in Figure S24.
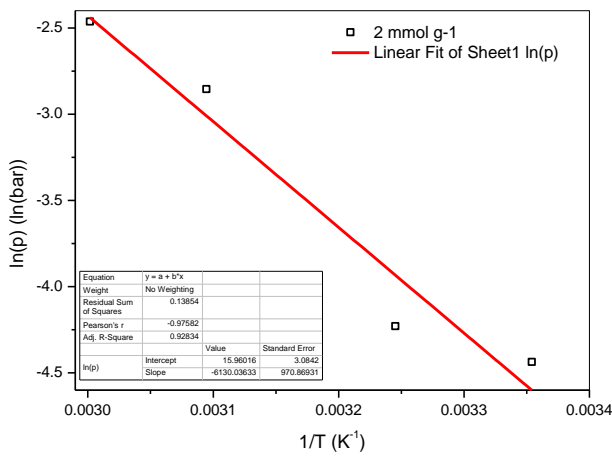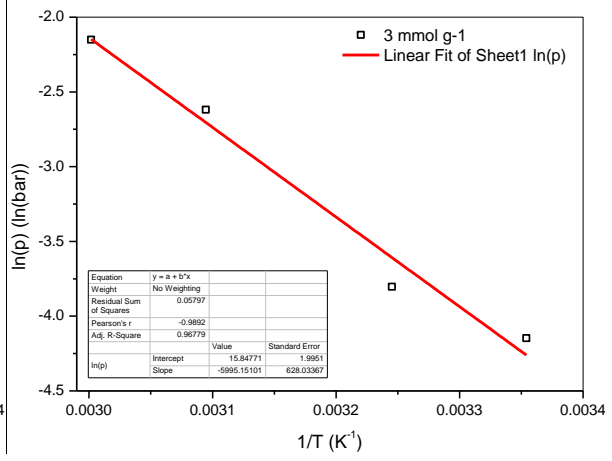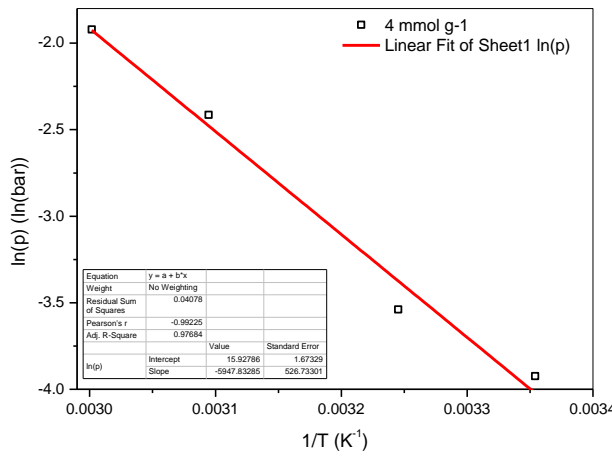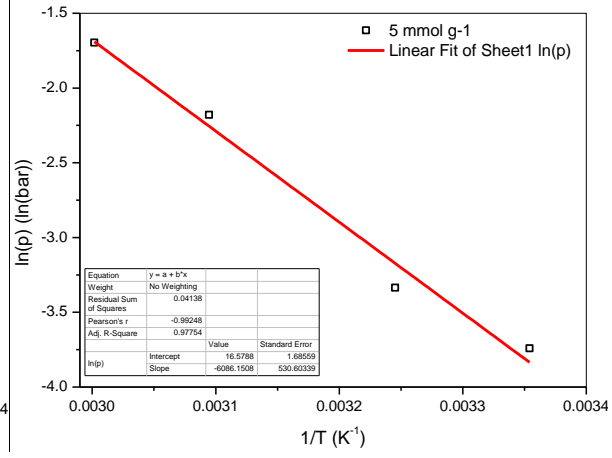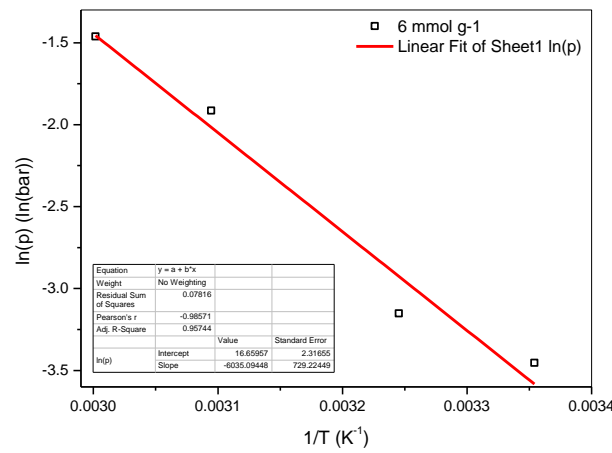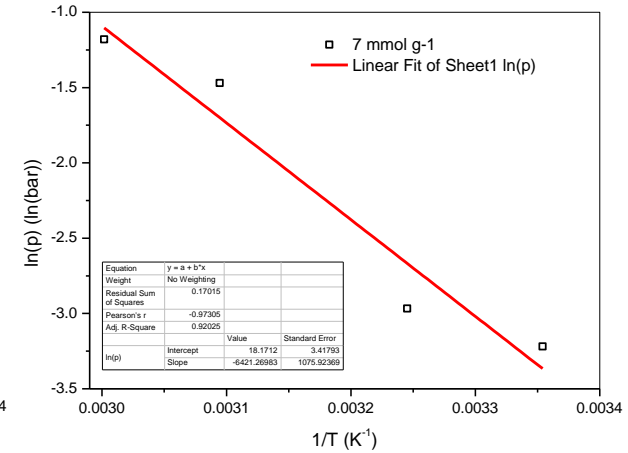
Figure S24. Linear fitting of Van't Hoff plots for the NO$_2$ adsorption isotherms at (a) 2.0, (b) 3.0, (c) 4.0, (d) 5.0, (e) 6.0 and (f) 7.0 mmol g^{-1} loading. [to de updated]

Table S5. Thermodynamic parameters for NO_2 adsorption in MFM-300(Al). [to de updated]

n mmol g^{-1}	Q_{st} kJ mol^{-1}	Q_{st} Err kJ mol^{-1}	ΔS J K^{-1} mol^{-1}	ΔS error J K^{-1} mol^{-1}	R^2
2	51.0	8.1	-132.7	25.6	0.9522
2.2	50.6	7.0	-132.2	22.3	0.9630
2.4	50.4	6.3	-132.0	19.9	0.9699
2.6	50.2	5.9	-131.9	18.7	0.9733
2.8	50.0	5.5	-131.8	17.6	0.9761
3	49.8	5.2	-131.8	16.6	0.9785
3.2	49.7	5.0	-131.8	15.8	0.9805
3.4	49.6	4.7	-131.9	15.1	0.9820
3.6	49.6	4.6	-132.1	14.7	0.9830
3.8	49.5	4.5	-132.2	14.3	0.9838
4	49.5	4.4	-132.4	13.9	0.9846
4.2	49.5	4.3	-133.0	13.6	0.9853
4.4	49.7	4.2	-133.8	13.3	0.9859
4.6	49.8	4.1	-134.5	13.1	0.9864
4.8	50.2	4.3	-136.3	13.5	0.9858
5	50.6	4.4	-137.8	14.0	0.9850
5.2	50.6	4.8	-138.1	15.1	0.9827
5.4	50.2	5.2	-137.5	16.6	0.9789
5.6	50.3	5.6	-137.9	17.8	0.9756
5.8	50.2	5.9	-138.3	18.7	0.9732
6	50.2	6.1	-138.5	19.3	0.9716
6.2	50.4	6.5	-139.7	20.6	0.9679
6.4	50.9	7.0	-141.8	22.2	0.9636
6.6	51.6	7.4	-144.3	23.7	0.9600
6.8	52.2	7.9	-146.7	25.2	0.9559
7	53.4	8.9	-151.1	28.4	0.9468
7.2	54.9	9.9	-156.4	31.5	0.9388
7.4	56.4	11.1	-161.9	35.3	0.9280
7.6	57.8	12.2	-166.8	38.7	0.9186
7.8	58.0	11.6	-167.6	36.9	0.9258
8	60.8	14.5	-177.6	46.0	0.8981

7.   Additional FTIR Spectra and analysis

a

b
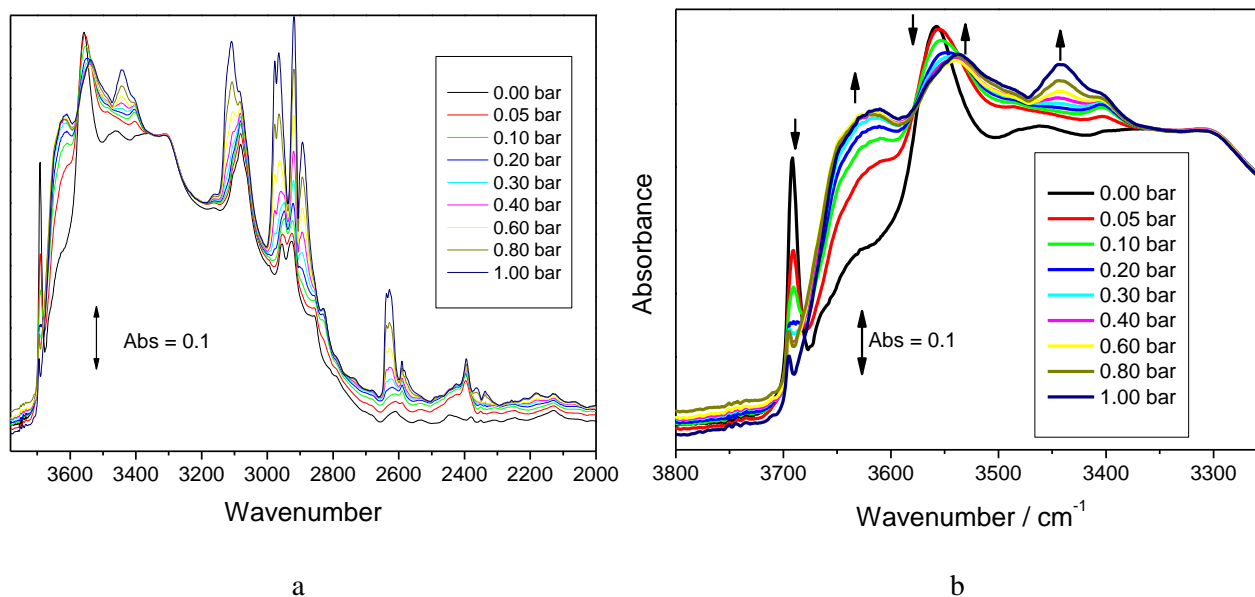
Figure S25. Fourier transform infrared spectroscopy (FTIR) for MFM-300(Al) as a function of NO$_2$ loading. *In situ* FTIR spectra of NO$_2$ and N$_2$O$_4$ molecules between 0.00 - 1.00 bar at 298 K with a sample of KBr + MFM-300(Al) (KBr background). The spectra at high wavenumbers (-OH region) are enlarged and shown in (b).

a

b
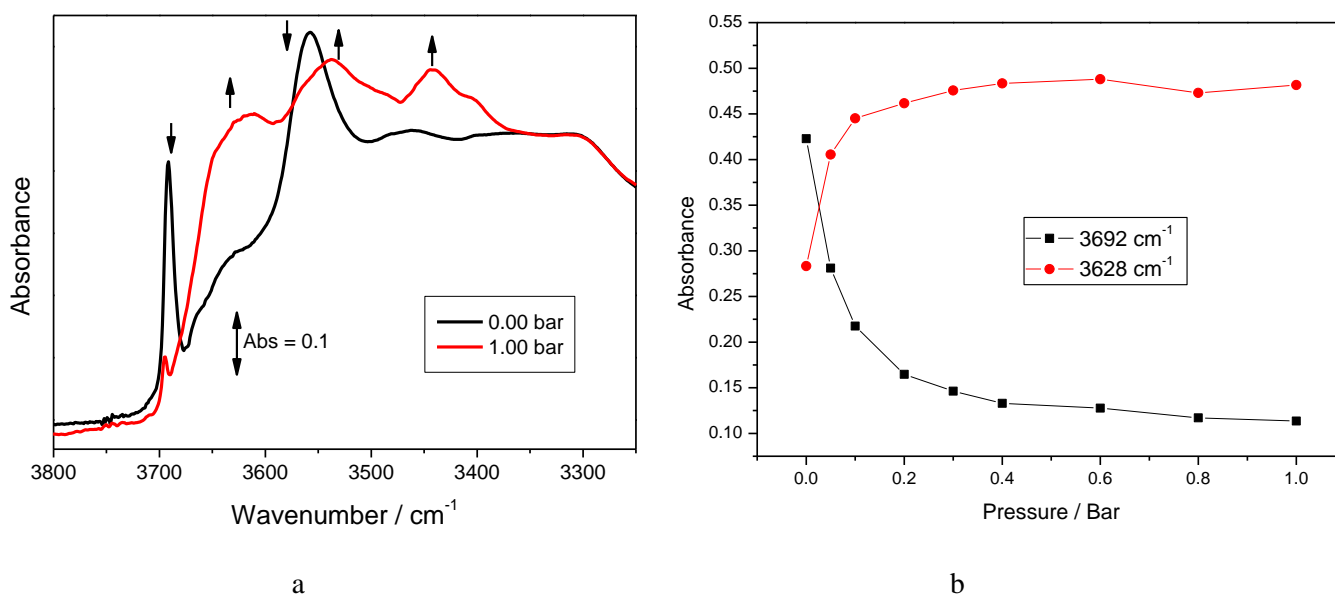
Figure S26. (a) Comparison of FTIR spectra for bare and NO$_2$-loaded MFM-300(Al) samples at 298 K showing the near-complete depletion of the –OH band at 3692 cm^{-1} as a result of NO$_2$ adsorption, further confirming the involvement of this hydroxyl group in binding of NO$_2$. (b) Variation of the band intensities for the peak at 3692 and 3628 cm^{-1} as a function of NO$_2$ pressure, confirming the formation of hydrogen bonds between the –OH group and adsorbed NO$_2$ molecules.

8.   Additional EPR Spectra and Analysis

8.1   Variable Temperature EPR Spectra

T / K
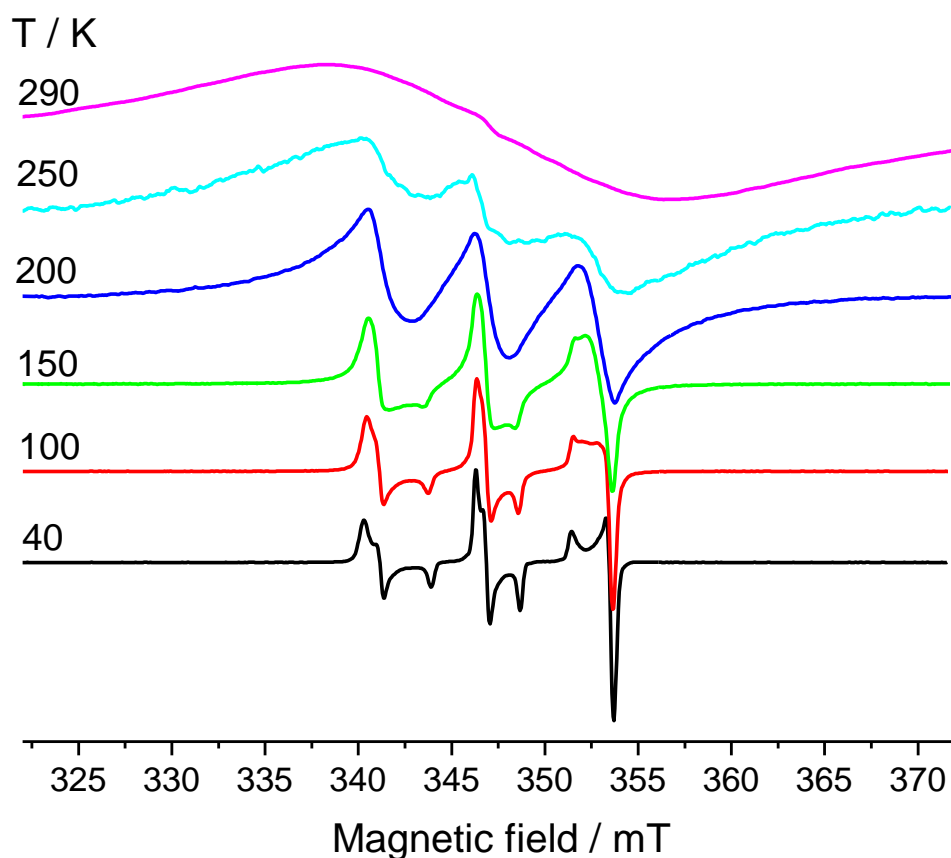
Figure S27. X-band EPR spectra of NO_2-loaded MFM-300(Al) at variable temperatures (40-290 K).

At temperatures below *ca.* 40 K the spectrum is essentially at the rigid limit, *i.e.*, the NO_2 molecule is immobilised. On warming to 100 K restricted slow motional effects are observed, and these are characteristic of preferential rotation of the adsorbed NO_2 about its molecular *y*-axis,[17] *i.e.,* parallel to the O…O vector. This direction is associated with the H-bond to the –OH group. At higher temperatures (above *ca.* 200 K) the spectrum simplifies to a three-line pattern indicating more isotropic motion. Note that the temperatures at which motional effects are observed are much higher than for NO_2 adsorbed onto powdered glasses, but similar to those for zeolite-adsorbed NO_2.[17]

8.2   Dipolar Model for ENDOR Calculations

ENDOR spectra show hyperfine interactions between the NO_2-based electron spin and ^1H nuclear spins of the interior of the MOF. To model the spectra and test the NO_2 binding site, we calculated the dipolar (through space) interactions between the NO_2 and the five nearest ^1H nuclei, *viz.* the –O$\underline{H}$ and four aromatic –C$\underline{H}$ groups (see above). The 3x3 dipolar ^1H hyperfine interaction matrices ($\mathbf{A}^{dip}$) were calculated according to:

$$\mathbf{A}^{dip} = \frac{\mu_0}{4\pi h}\beta_e\beta_n \frac{3(\mathbf{g}.\mathbf{n})(\tilde{\mathbf{n}}.g_H\mathbf{1}) - \mathbf{g}.g_H\mathbf{1}}{r^3}$$

where **g** and $g_H\mathbf{1}$ are the electron and ^{1}H nuclear **g** matrices ($g_H = 5.586$; **1** is the unit matrix), r is the $\underline{N}O_2$…H distance, **n** is the $\underline{N}O_2$…H unit vector expressed in the NO_2 molecular reference frame, and **ñ** is its transpose; h is Plank's constant, μ_0 is the vacuum permittivity, β_e is the Bohr magneton and β_n is the nuclear magneton. The **g**-matrix is known from the EPR spectrum. The NO_2 molecular reference frame was defined as the principal axes of the C_{2v} symmetry NO_2 molecule, with which the molecular **g** and $\mathbf{A}_N$ (the ^{14}N hyperfine matrix of NO_2) axes are coincident:

z: parallel to the C_2 axis of NO_2, calculated as the unit vector between N and the midpoint of the O…O atoms;

y: parallel to the O…O direction, calculated as the unit vector;

x: perpendicular to the plane of the NO_2 molecule, calculated as the cross-product of the y and z unit vectors.

The relationship of the **g**-matrix principal values and this axis system for the NO_2 free-radical (trapped in various media) is well established;[16] our values of $g_x = 2.0052$, $g_y = 1.9915$, $g_z = 2.0021$ (Fig. 4) are typical.

The vectors **n** are given by $\begin{pmatrix} \cos\alpha \\ \cos\beta \\ \cos\gamma \end{pmatrix}$ where α, β and γ are the angles of the $\underline{N}O_2\cdots$H vectors to the molecular NO_2 axes.

We initially used the DFT-optimised atomic coordinates from PXRD to calculate r, α, β and γ for each of the five ^{1}H nuclei (Table S5; using the $\underline{N}O_2$ atom coordinate, since this carries the bulk of the electron spin density). This gave reasonable spectra, but with the absolute values of the hyperfine coupling constants varying by up to *ca.* 10 % of the experimental values. Because of the r^{-3} dependence this corresponds to very small changes in inter-nuclear distances (*ca.* 0.1 Å change in r of 3 Å; for the same reason the calculated ENDOR spectra are much more sensitive to small changes in r than small changes in α, β, γ). Hence, we explored translations of the NO_2 coordinates within a very limited range in the fixed site I binding site, with recalculation of the r values (hence, the five r values are *not* treated as independent variables). Good agreement is found with the experimental ENDOR spectra with the r values in Table S6. For example, we find a $\underline{N}O_2$...O$\underline{H}$ distance of 3.1 Å, compared to the 2.9 given by the DFT-optimised PXRD model. In order to get a good simultaneous agreement to the x, y and z orientation selective data (Figure 4, main text) we found it necessary to introduce a rotation of the NO_2 about its molecular y axis (of 50º, with respect to the orientation in the DFT-optimised structure). This is the easiest axis of rotation for the bound molecule (see above) and hence it is possible that a range of orientations could be present in the lattice. It is also possible that this is responsible for the minor discrepancies in the relative transition intensities for the z orientation selective spectrum (which we find to be most sensitive to the rotation angle). In summary, the ENDOR spectra are conclusive in confirming the NO_2 site I binding model, with only minor changes in position from the DFT/PXRD solutions. ENDOR spectrum calculations based on the structure solution direct from PXRD (with positional disorder and without DFT refinement) gave much poorer agreements.

Table S6. Structural parameters from DFT-refined PXRD structure, and used for calculation of ENDOR spectra. N is the $\underline{N}O_2$ atom of the site I adsorbed NO_2 monomer.

	DFT N⋯H distance, r / Å	ENDOR N⋯H distance, r / Å	α / degrees	β / degrees	γ / degrees
–OH	2.889	3.09	71	159	94
–CH[a]	3.021	3.09	70	110	30
–CH[b]	3.203	3.54	63	115	140
–CH[c]	3.529	3.49	100	117	150
–CH[d]	3.756	3.62	96	141	51

9. Analytical fitting of the adsorption isotherms by dual-site Langmuir-Freundlich model

The adsorption isotherms of NO_2, SO_2, CO_2 and N_2 in MFM-300(Al) at 298 K were fitted using a dual-site Langmuir-Freundlich model (equation 2), where n is the amount adsorbed in mmol g^{-1}, P is the pressure in bar, $q_{sat,i}$ is the saturation capacity in mmol g^{-1}, b_i is the Langmuir parameter in bar^{-1}, and v_i is the Freundlich parameter for two sites 1 and 2. High pressure isotherms have been used for CO_2 and N_2 to include an extended surface coverage for the fitting and thus to reduce the uncertainty for the sequential IAST analysis. The fitted parameters for each adsorption isotherm are listed in supplementary Table S7. Comparison of the adsorption isotherms and the corresponding dual-site Langmuir-Freundlich fits are shown in Supplementary Figure S28. The regression coefficients are all above 0.999 for the NO_2, SO_2, CO_2 and N_2 adsorption data of MFM-300(Al), confirming that the model fits the data very well.

$$n = \frac{q_{sat1}b_1 P^{v_1}}{1 + b_1 P^{v_1}} + \frac{q_{sat2}b_2 P^{v_2}}{1 + b_2 P^{v_2}}$$

(2)

IAST is widely used in the field of MOFs to estimate the selectivity data based upon pure component isotherms. To simplify the IAST calculation, ideally the pure-component adsorption isotherms need be fitted empirically by an analytic equation.[18] The widely-applied Langmuir double site model is used here. However, strictly speaking, adsorption of NO_2 in MFM-300(Al) cannot be described accurately by Langmuir model because (i) the solid surface is not uniform (presence of strong binding site); (ii) there is significant gas-gas binding interaction with bond formation (dimerization). As a result, physical meanings extracted from the analytic fitting cannot be directly compared with the PXRD/FTIR results. The model is only used here as an analytic solution to simplify the IAST calculation.[18]
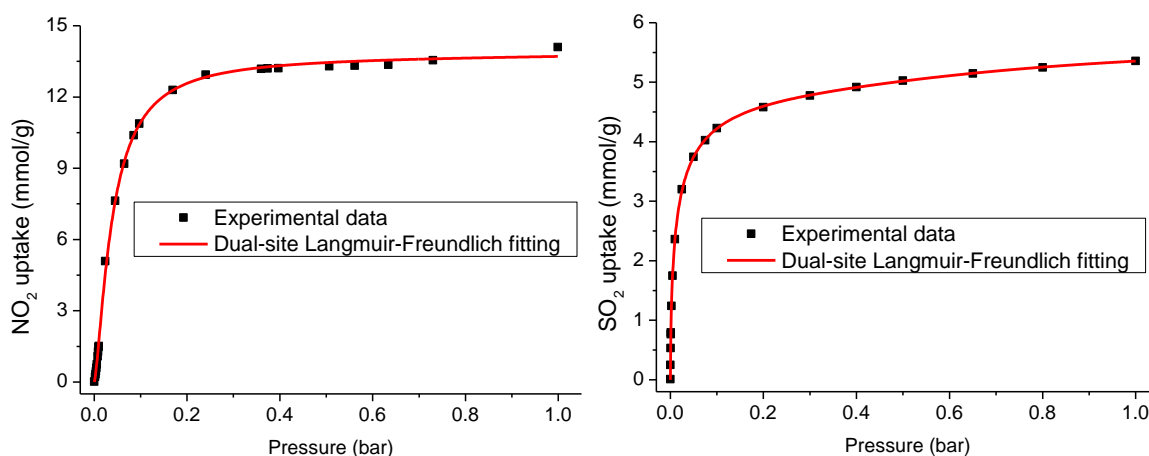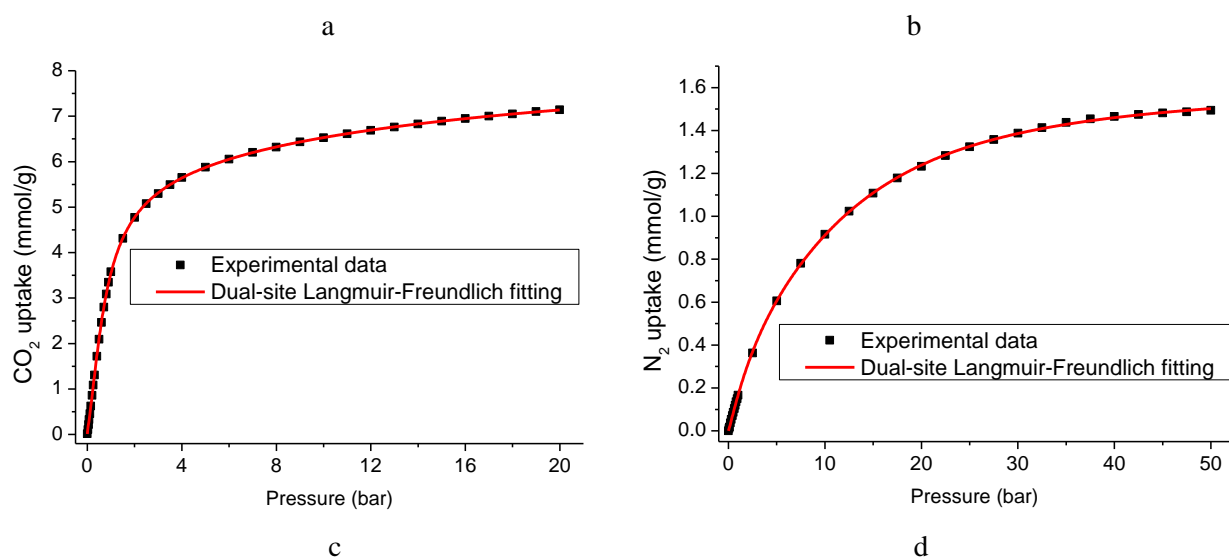
Figure S28. Dual-site Langmuir-Freundlich fitting for (a) NO_2, (b) SO_2, (c) CO_2 and (d) N_2 adsorption isotherms in MFM-300(Al) at 298 K.

Table S7. Summary of dual-site Langmuir-Freundlich fitting parameters for NO_2, SO_2, CO_2 and N_2 derived from the adsorption isotherms in MFM-300(Al) at 298 K.

	NO_2	SO_2	CO_2	N_2
q_{sat1} (mmol g^{-1})	13.79	5.385	5.504	1.021
b_1 (bar^{-1})	103.8	16.728	0.211	0.189
v_1 (dimensionless)	1.434	0.665	0.604	1.106
q_{sat2} (mmol g^{-1})	4.583	0.393	4.054	0.601
b_2 (bar^{-1})	0.011	2.283	1.769	0.005
v_2 (dimensionless)	2.734	2.745	1.663	1.924
R^2	0.9990	0.9999	0.9999	0.9999
Residual	0.0033	6.3e^{-4}	1.9e^{-4}	2.0e^{-5}

10.   IAST Analysis of the selectivity data of hydrocarbon adsorption in MFM-300(Al)

Ideal adsorbed solution theory (IAST)[18] was used to determine the selectivity factor, S, for binary mixtures using pure component isotherm data. The selectivity factor, S, is defined according to Equation 3 where x_i is the amount of each component adsorbed as determined from IAST and y_i is the mole fraction of each component in the gas phase at equilibrium. The IAST adsorption selectivities were calculated for equimolar binary mixtures of NO_2/SO_2, NO_2/CO_2 and NO_2/N_2 at 298 K and at a pressure range of 0.1-1 bar. The selectivity of NO_2/N_2 is subject to large uncertainties associated with isotherm measurement of the extremely low N_2 uptake in MFM-300(Al) and the NO_2/N_2 selectivity is reported as > 10,000 in this report. The accuracy of the IAST analysis starts to decay when (i) strong binding sites appear on the pore surface of the host material (*i.e.,* the pore surface is not homogenous), and (ii) in the gas mixture one component is much more strongly adsorbed than the other.[18] Analysis of IAST adsorption selectivity carries very large uncertainties at the low pressure region due to the low isotherm uptake (and hence low spreading pressure). We therefore carried out the IAST calculation from 0.1 to 1.0 bar only, where the isotherm uptake affords a reasonable integration of the spreading pressure. These selectivity data are shown in Supplementary Figure S25.

$$S = \frac{x_1 / y_1}{x_2 / y_2} \qquad\qquad (3)$$
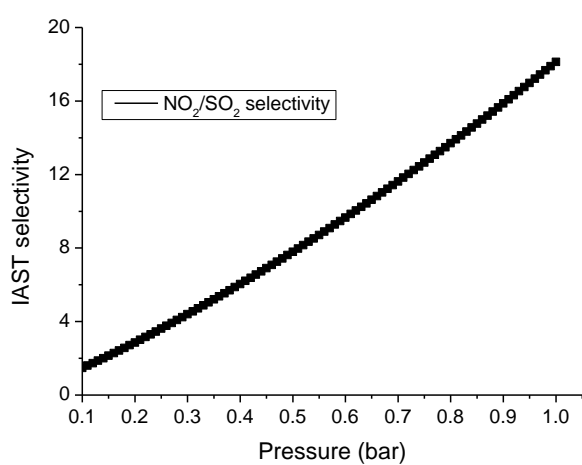
a
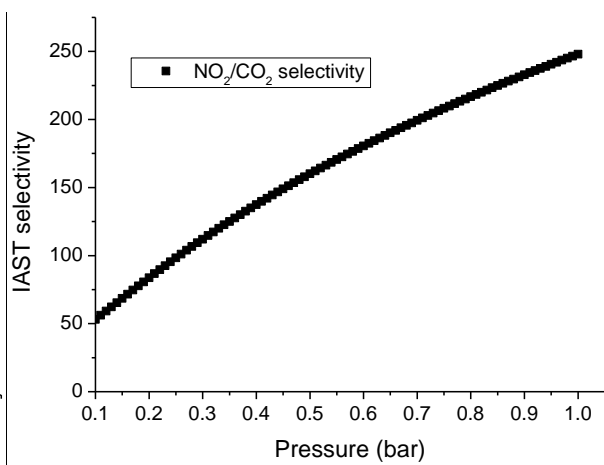
b
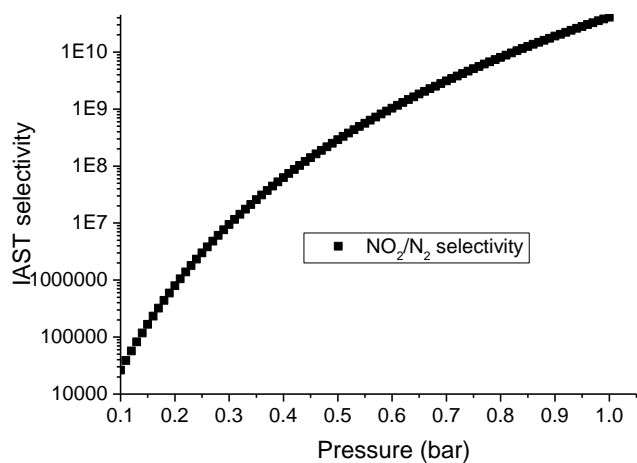
c

Figure S29. IAST selectivities for equimolar binary mixtures of (a) NO_2 and SO_2, (b) NO_2 and CO_2, (c) NO_2 and N_2 of varying pressures (0.1-1.0 bar) at 298 K.

11.   Breakthrough Experiments

To further evaluate the performance of MFM-300(Al) for the adsorptive removal of low concentration NO_2 under both dry and wet conditions, breakthrough experiments were performed in which a stream of 0.5% NO_2 (*i.e.*, 5000 ppm) diluted in He and N_2 was flowed through a packed bed of MFM-300(Al) (approximately 3 g) at a total flow of 40 mL/min at 298 K and 1.0 bar. Same experiment were repeated under wet conditions in presence of water vapour in the gas stream. As suggested from pure component isotherms and selectivity calculations, MFM-300(Al) has strong adsorption affinity and high capacity to NO_2. In the breakthrough experiment, N_2 was the first to elute through the bed at t = 9 minutes, with NO_2 selectively retained. Upon saturation, NO_2 broke through from the bed and reached saturation rapidly at t = 253 minutes. As measured from this breakthrough experiment, for an entering 5000 ppm NO_2 feed, the concentration of NO_2 at the outlet is found below the detection limit (< 1 ppm) before the breakthrough. The retention of NO_2 in MFM-300(Al) under wet conditions has also been confirmed with a minor reduction on the breakthrough time due to the presence of competitive adsorption with water. Desorption of breakthrough curve was measured after adsorption under a flow of dry He at a rate of 13 mL/min at 298 K and 1 bar. A lower flow rate was used for desorption is to avoid the presence of intensive turbulence caused by initially rapid desorption to mass spectrometer and therefore to enable the record of complete desorption curve steadily. It is worth noting that the desorption conditions used here are very mild and not directly comparable with that used in practical processes *via* either temperature-swing or pressure-swing operations.

Dimensionless breakthrough plots were also calculated with the following parameters: bed diameter, *d*, (7 mm), bed length, *L*, (120 mm), flow rate (40 mL/min unless otherwise noted), bed volume (5 mL), sample mass (3.0 g), sample framework density (1.06 g/cm^3). The sample occupies a volume of 2.83 mL (assuming 100% purity and no framework collapse), and thus the fractional porosity of the fixed bed, ε, is calculated to be 0.434. The superficial gas velocity, *u*, at the entrance of the bed corresponds to $1.73e^{-2}$ m/s. The characteristic contact time between the gas and the MFM-300(Al) samples, $\varepsilon L/u$ = 3.01 s. The dimensionless time, τ, was obtained by dividing the actual time, *t*, by the contact time between the gas and the MFM-300(Al) sample, $\varepsilon L/u$, *i.e.* $\tau = tu/\varepsilon L$.
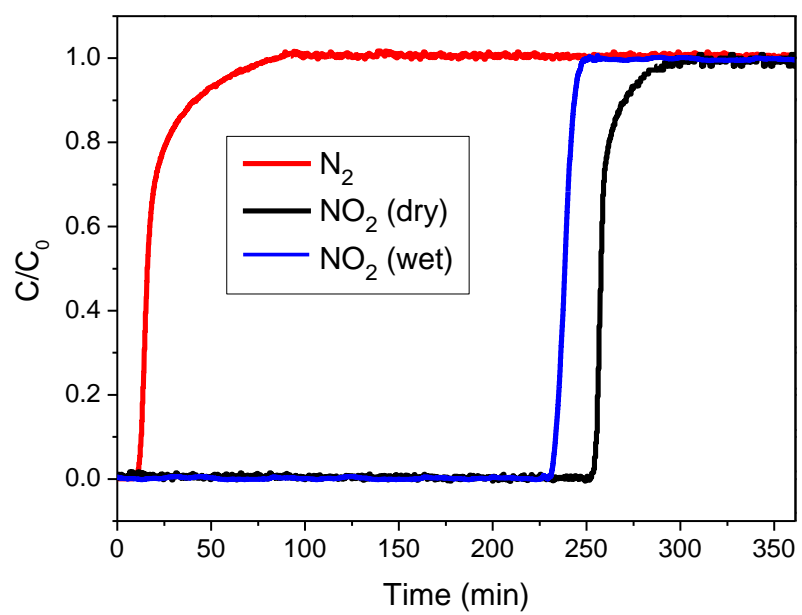
Figure S30. Breakthrough plot for 0.5 % NO_2 (5000 ppm) in He/N_2 through MFM-300(Al) under dry and wet conditions at room temperature (298 K) and atmospheric pressure.
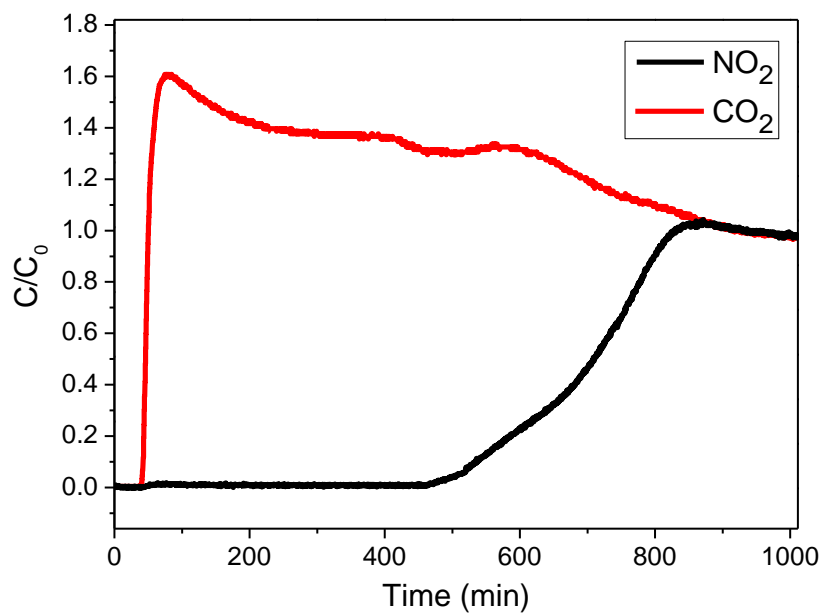
Figure S31. Breakthrough plot of 0.4% NO_2 (4000 ppm) and 15% CO_2 (v/v) diluted in He in a fixed-bed packed with MFM-300(Al) at room temperature (298 K) and atmospheric pressure (total flow rate 47 mL/min). 15% CO_2 was selected to simulate flue gas composition.
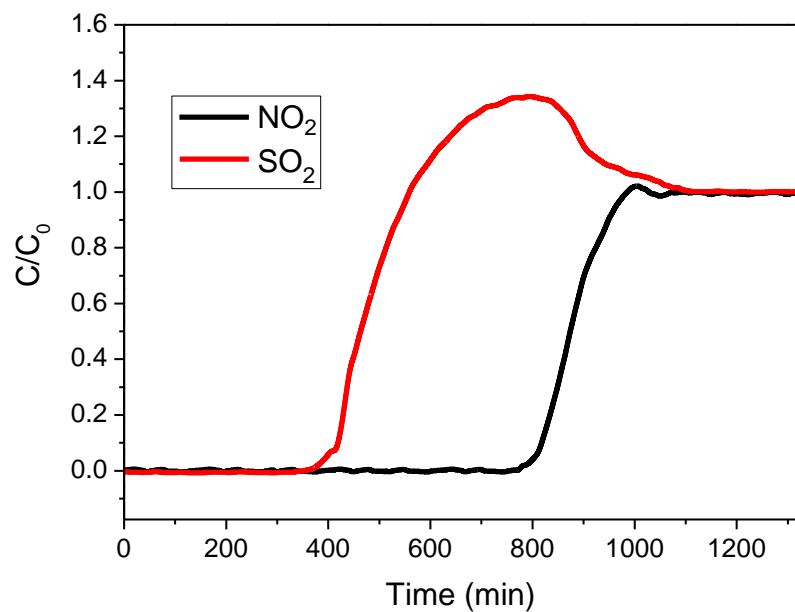
Figure S32. Breakthrough plot of 0.16% NO_2 (1666 ppm) and 0.34% SO_2 (3334 ppm) diluted in He in a fixed-bed packed with MFM-300(Al) at room temperature (298 K) and atmospheric pressure (total flow rate 19 mL/min).
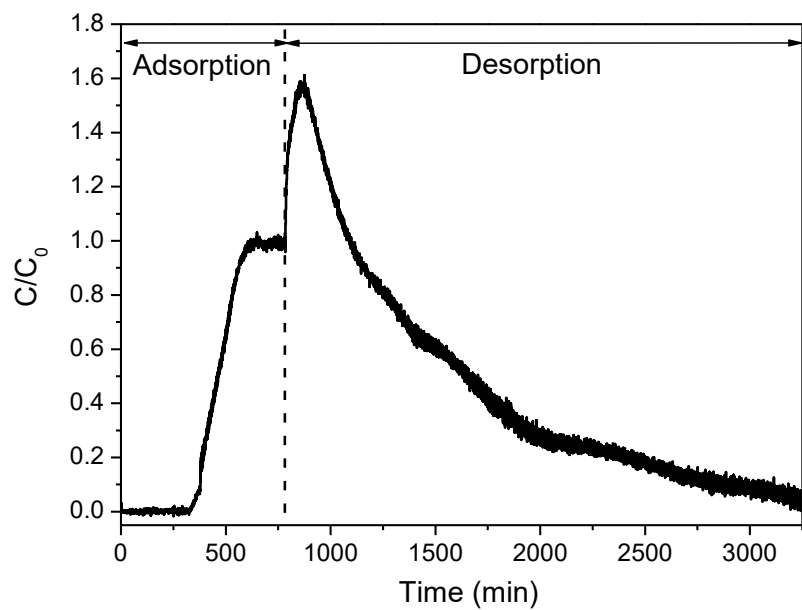
Figure S33. Breakthrough plot for 0.5% NO_2 (5000 ppm) in a flow of He at 40 mL/min through MFM-300(Al) at room temperature (298 K) and atmospheric pressure and desorption branch at a flow of pure He at 13 mL/min at 298 K and atmospheric pressure.

12. References:

1 Yang, S. *et al.* Selectivity and direct visualization of carbon dioxide and sulfur dioxide in a decorated porous host. *Nat. Chem.* **4**, 887-894 (2012).

2 Cooper, A. I. & Poliakoff, M. High-pressure reactions in polyethylene films, a new development in matrix isolation. The photochemical reaction of $Fe(CO)_5$ with N_2 and the thermal reaction of $Fe(CO)_4(N_2)$ with H_2. *Chem. Phys. Lett.* **212**, 611-616 (1993).

3 Clark, S. J. *et al.* First principles methods using CASTEP. *Z. Kristall.* **220**, 567-570 (2005).

4 Ramirez-Cuesta, A. J. aCLIMAX 4.0.1, The new version of the software for analyzing and interpreting INS spectra. *Comput. Phys. Commun.* **157**, 226-238 (2004).

5 Rietveld, H. M. A profile refinement method for nuclear and magnetic structures. *J. Appl. Crystallogr.* **2**, 65-71 (1969).

6 A. Schweiger and G. Jeschke, *Principles of Pulse Electron Paramagnetic Resonance*; Oxford University Press (2001).

7 Stoll, S. and Schweiger, A. EasySpin, a comprehensive software package for spectral simulation and analysis in EPR. *J. Magn. Reson.* **178**, 42-55 (2006).

8 Stoll, S. & Britt, R. D. General and efficient simulation of pulse EPR spectra. *PCCP* **11**, 6614-6625 (2009).

9 J. G. Bell, S. A. Morris, F. Aidoudi, L. J. McCormick, R. E. Morris & K. M. Thomas, Physisorption-induced structural change directing carbon monoxide chemisorption and nitric oxide coordination on hemilabile porous metal organic framework $NaNi_3(OH)(SIP)_2(H_2O)_5 \cdot H_2O$ (SIP = 5-sulfoisophthalate). *J. Mater. Chem. A.* **5**, 23577-23591 (2017).

10 Peterson, G. W., Mahle, J. J., DeCoste, J. B., Gordon, W. O. & Rossin, J. A. Extraordinary NO_2 removal by the metal–organic framework UiO-66-NH_2. *Angew. Chem. Int. Ed.* **55**, 6235-6238 (2016).

11 Levasseur, B., Petit, C. & Bandosz, T. J. Reactive adsorption of NO_2 on copper-based metal−organic framework and graphite oxide/metal−organic framework composites. *ACS Appl. Mater. Interfaces* **2**, 3606-3613 (2010).

12 Petit, C., Levasseur, B., Mendoza, B. & Bandosz, T. J. Reactive adsorption of acidic gases on MOF/graphite oxide composites. *Microporous Mesoporous Mater.* **154**, 107-112 (2012).

13 Ebrahim, A. M., Levasseur, B. & Bandosz, T. J. Interactions of NO_2 with Zr-based MOF: effects of the size of organic linkers on NO_2 adsorption at ambient conditions. *Langmuir* **29**, 168-174 (2013).

14 DeCoste, J. B., Demasky, T. J., Katz, M. J., Farha, O. K. & Hupp, J. T. A UiO-66 analogue with uncoordinated carboxylic acids for the broad-spectrum removal of toxic chemicals. *New J. Chem.* **39**, 2396-2399 (2015).

15 Ebrahim, A. M. & Bandosz, T. J. Effect of amine modification on the properties of zirconium–carboxylic acid based materials and their applications as NO_2 adsorbents at ambient conditions. *Microporous Mesoporous Mater.* **188**, 149-162 (2014).

16 Ebrahim, A. M. & Bandosz, T. J. Ce(III) Doped Zr-based MOFs as excellent NO_2 adsorbents at ambient conditions. *ACS Appl. Mater. Interfaces* **5**, 10565-10573 (2013).

17 Shlotani, M. and Freed, J. H. ESR studies of NO_2 adsorbed on surfaces: analysis of motional dynamics. *J. Phys. Chem.* **85**, 3873-3883 (1981).

18 Myers, A. L. & Prausnitz, J. M. Thermodynamics of mixed-gas adsorption. *AlChE J.* **11**, 121-127 (1965).